Theoretical and Applied Fracture Mechanics 96 (2018) 658–675

Contents lists available at ScienceDirect

Theoretical and Applied Fracture Mechanics

journal homepage: www.elsevier.com/locate/tafmec

Ductile tearing analysis of TC128 tank car steel under mode I loading condition

Marcelo Paredes[a,*], Diego F.B. Sarzosa[b], Rafael Savioli[b], Tomasz Wierzbicki[a], David Y. Jeong[c], David C. Tyrell[c]

[a] Impact and Crashworthiness Laboratory, Massachusetts Institute of Technology, Cambridge, MA 02139, USA
[b] Department of Ocean Engineering and Naval Architecture, University of Sao Paulo, Sao Paulo, SP 05508-030, Brazil
[c] Volpe National Transportation Systems Center, Cambridge, MA 02139, USA

ABSTRACT

The objective of the present work is to incorporate the effect of post-failure softening on fracture initiation modeling of steel alloy TC128 commonly used in railroad tank car manufacturing. The fracture initiation process is determined through a comprehensive mechanical tests, which includes tensile tests on standard dog-bone specimens, flat specimens with circular cutouts and central hole, notched round bars, punch indentation tests on circular blanks and special flat shear specimens. Ductile fracture toughness usually referred to as resistance curve is measured from two types of typical fracture mechanics specimen geometries: the compact tension C(T) and the three-point bending SE(B). Post-failure softening is then coupled with the constitutive model to describe ductile fracture propagation. It turns out that in the absence of softening in fracture, the crack growth rate increases with little resistance opposite of what has been observed in fracture response of typical steels. On the other hand, the post-failure softening algorithm increases the ductile resistance behavior of the material more realistically, compared to experiments and provides additional information regarding the state of stress governing the fracture process.

1. Introduction

Hazardous material transportation by means of hauled railroad tank cars is a frequent operation taken on daily basis across United States. Even though accident index of train collision or derailment has remained low over the past years, its catastrophic incidence against environment might be irreversible due to spilling of toxic materials [1–4]. The common critical locations where those releases occur have been reported in the head (end caps), body (shell) and valve fittings of the tank car [5,6]. The post-accident examinations of crashed tank car surfaces indicated that the predominantly failure mechanism is ductile fracture accompanied by some brittle features [7,8]. It is worthy to mention that those accidents involved tank cars built with non-normalized steels, which exhibit lower ductile-brittle transition and potentially lower fracture toughness [8]. Due to modifications in Federal regulation regarding tank car safety, normalized steels were proposed for pressurized containers construction. Thus, testing protocols and guidelines for material characterization were proposed in order to insure safety and survivability [9,10].

Since impact loads are involved during train collision, the material characterization procedure adopted by railroad industry relies heavily on charpy experiment only as a key testing procedure to determine mechanical response of the material. Even though charpy test provides reliable information about impact energy at different temperature ranges and ductile/brittle transition points, but still brings so little about ductile tearing behavior. A recent study performed by Southwest Research Institute (SwRI) on a series of tank car steels extracted from decommissioned railroad cars reveals sustained ductile tearing growth in standard compact tension C(T) specimens subjected to high rate loading and low temperature [8]. The testing protocol used for material characterization was entirely based on linear elastic fracture mechanics and energy impact approaches. It turns out that even having low temperature range (0° to −50°F) the required fracture energy for TC128-B was higher than the one expected for such conditions (large plastic zone size accompanied by shear lips and splitting), which implies that the fracture toughness measures does not necessarily represents a material property. This put an important question on the table about the reliability of each available engineering approach to evaluate failure behavior and structural integrity of railroad equipment. Despite the strong evidence of ductile fracture mechanism observed during experiments,

* Corresponding author.
E-mail address: lparedes@mit.edu (M. Paredes).

https://doi.org/10.1016/j.tafmec.2017.10.006
Received 7 April 2017; Received in revised form 14 September 2017; Accepted 23 October 2017
Available online 08 November 2017
0167-8442/

the study lacks ductile tearing tests to determine crack driving forces to extend a pre-existing crack stably a few millimeters before turning unstable. This type of test will provide important information about the fracture toughness as well as tearing resistance of a given structure under monotonic loading condition.

The well-known mechanism of ductile fracture under mode I loading distinguishes three different stages of evolving voids: nucleation, growth and coalescence. Voids are usually generated by decohesion or cracking of second phase particles embedded in the matrix material [11–13]. The state of stress and the loading history plays an important role in defining the shape of cavities until coalescence occurs assisted for additional secondary submicron-sized inclusions. Several porous material models have been proposed over the years based initially upon the fundamental work of Gurson [14], where an initial idealized spherical/cylindrical void evolves under straining following a suitable nucleation, growth and coalescence (at certain extent) criteria to complete the constitutive description of porous media [15–20]. Applications on predicting ductile crack propagation in fracture mechanics specimens using this approach, historically, have long been performed by many researchers, being relevant the works of Xia and Shih (X&S) [21–24], Ruggieri et al. [25], Sun et al. [26], Brocks et al. [27] among others. X&S, basically, proposed a computational cell modeling technique at which the fracture process develops allowing the crack advances once a critical stage in a cell is attained. Upon experimental observations [28–31], initiation and stable ductile tearing propagation depend strongly on geometry and loading condition. The crack-tip conditions dictate the level of constraint at which the material point near the crack is stressed and become the driving force behind the fracture process. There exist a strong nonlinear coupling between this fracture process, where voids grow, with plastic dissipation in the background material (remaining ligament) as postulated by Tvergaard and Hutchinson [32] and Shih and Xia [33]. The latter introduced a discrete form to represent the fracture process zone by a collection of computational cells (cubic elements) operationally located on the plane by which the crack will propagate. The characteristic dimensions of each cell must agree with physical size scale relevant to microstructural fracture processes [34].

The computational cell scheme was further rationalized in a series of two papers by Faleskog et al. [35,36], where the calibration process of Gurson-type model is divided in two steps: micromechanics and fracture process parameters calibration. While the former relies heavily upon finite element analysis to determine controlling parameters for nucleation and growth of a single void-containing representative volume element (RVE), the latter requires crack growth resistance data from standard fracture toughness experiments. It is clear from these analyses that the fracture process does not depend on the mechanism of the void growth solely but also its interaction with the surrounding material and distribution of inclusions in the matrix. Some examples of its implementation in flawed structural problems might be seen in Ruggieri and Dotta [37], Sarzosa and Ruggieri [38], Tanguy et al. [39] or in dynamic applications of high pressurized line pipes studied by Scheider et al. [40]. These studies reveal the robustness of the underlying scheme to transfer damage parameters from lab scale test to large scale problems.

A parallel line of research which involves physical-based local failure criteria with uncoupled plasticity models have become an attractive alternative due to its simplicity in computational implementation and experimental calibration procedure [41–45]. The key feature of it is that damage is accounted for as an external state variable without affecting elastic-plastic constitutive equations. The limit of ductility or the onset of fracture is considered when the accumulative incremental damage indicator attains a critical value. As a result the global mechanical response (load-displacement curve) would be influenced by a suddenly or gradually drops in the load, marking the initiation of fracture at lab scale tests. For instance, in some recent publications related to tank car collisions the use of a Bao-Wierzbicki (B-W) phenomenological failure model [6,7,46,47] has been satisfactory to determine global force-indentation characteristics. Basically, B-W predicts fracture initiation through a set of three-empirical branches defined by equivalent plastic strain and stress triaxiality [48]. One of the main advantages of this phenomenological model is the capability to predict failure where the void volumetric dilatancy is not possible to occur but distortional (shearing) mechanism does instead. But, on the other hand, this damage criterion is confined to 2D settings only which make its usage appropriate for plane stress problems. Since membrane stresses are mainly present in thin-walled tanks, out-of-plane stress components are almost negligible at the instant of impact of a speedy ram against body. This simplifies the complexity of a three dimensional problem into a bi-dimensional one by making the global response simulation tractable. In reality, the newly created fracture surface after puncture depends strongly on the actual crack-tip conditions and will define the path and rate of propagation [49,50].

However, earlier experiments using several small scale specimens with different geometries and material properties reveal the dependence of third invariant of stress deviator on fracture behavior [51–53]. This fact motivated Bai and Wierzbicki [54] to extend the applicability of the original Mohr-Coulomb criterion (widely used by rock and soil mechanics) to predict the onset of fracture in ductile materials. The modified Mohr-Coulomb (MMC) represents a decomposition of the original scheme in terms of stresses into a mixed 3D representation of equivalent strain to fracture, stress triaxiality and normalized lode angle ($\bar{\varepsilon}_f,\eta,\bar{\theta}$). For a proportional loading, the 3D fracture surface exhibits an asymmetric trend regarding of lode angle (normalized third invariant of stress deviator tensor) and exponential decay with respect to stress triaxiality [54]. Moreover, Mohr and Marcadet [56] proposed a micromechanically based phenomenological Hosford-Coulomb (HC) model to predict ductile fracture initiation in low stress triaxialities problems. They were initially inspired by the findings of Dunand and Mohr [77], where the predictive capability of MMC was put to the test by comparing with the results obtained from GTN model. It turns out that MMC fracture criterion offers a slight advantage over the latter for low stress triaxiality levels. The Mohr's approach was devised as a localization criterion for fracture initiation in ductile materials by replacing the Tresca equivalent stress with the Hosford equivalent stress. In particular, this work removes some internal inconsistencies found in the mathematical formulation of the MMC model upon transformation to the mixed strain-stress space.

The present work follows up the exploratory work initiated by Kofiani et al. [62] and Paredes et al. [55] in using the MMC fracture criterion –originally developed for sheet metal problems- to predict crack propagation in standard fracture mechanics specimens. The selected sample geometries are three-point bending single edge notch SE (B) and compact tension C(T) specimens. Through the use of the abovementioned phenomenological approach along with suitable post-failure softening algorithm to account for progressively material strength degradation, ductile tearing response in TC128 steels is predicted and compared with experiments.

2. Material and experiments

The tested material is a typical railroad tank car steel coded as TC128. A circular plate was extracted directly from the top of a decommissioned tank car as shown in Fig. 1. Due to the shell heavy wall-thickness (~40 mm) the samples intended for mechanical tests were extracted from the core base material in a remotely region away from the girth weld (circumferential weld). Two sets of specimens were prepared for fracture initiation and propagation, respectively. The former are comprised by a series of different flat geometries for tension and shear tests in which plasticity and the onset of failure properties of the material are determined. Meanwhile, fracture propagation parameters are computed from typical geometrically constrained fracture mechanics specimens as depicted in Fig. 1c. The flat specimens were

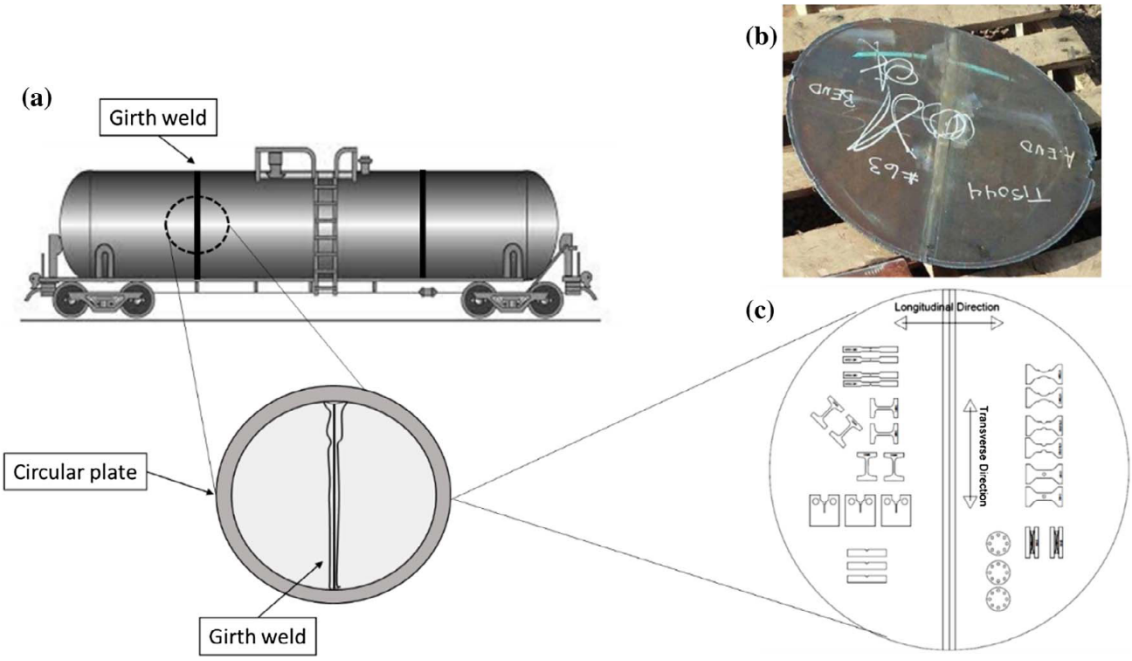

Fig. 1. (a) Schematic representation of railroad tank car and extracted plate; (b) TC128 circular plate and (c) general layout of specimens used for material characterization.

machined out from the plate by Computer Numerical Control (CNC) process until the desire thickness is achieved (~2 mm) and water jet/mill technique for shaping and polishing the geometries. Due to large tank radius-to-thickness ratio, the curvature was negligible at specimen level, thus straightness was ensured. Since lateral collision with moving ram is considered for the present analysis, the acting stresses are more significant along the longitudinal than transverse direction. Therefore, all the samples were oriented along the longitudinal for material characterization except uniaxial tensile specimens, which were extracted in three different material orientations for anisotropy assessment. The selected directions were longitudinal (0°), diagonal (45°) and transverse (90°) with respect to the axial reference of the tank car as shown in Fig. 1c.

Uniaxial tensile test results and plastic strain evolution of width vs. thickness of specimens are depicted in Fig. 2a and b, respectively. The material exhibits a moderate Lüders plateau in the elastic-plastic transition as a result of manufacturing process with an almost in-plane isotropic behavior according to Fig. 2b. The slope of the evolution of plastic strain width against plastic strain thickness is the measure of the amount of anisotropy. If the material exhibits a Lankford ratio (slope) near to unity, the material it says is isotropic, otherwise, it is anisotropic. Based on Table 1, the current TC128 is assumed isotropic, although it exhibits a slightly anisotropic dependence along 90°.

Table 1
Mechanical properties of TC128 tank car steel at room temperature.

Young's modulus E (MPa)	Poison's ratio ν	Material orientation deg (°)	Yield stresses σ_y (MPa)	Tensile stresses σ_u (MPa)	Lankford ratio (–)
210,000	0.3	0	428	639	0.95
		45	428	638	1.01
		90	430	636	0.93

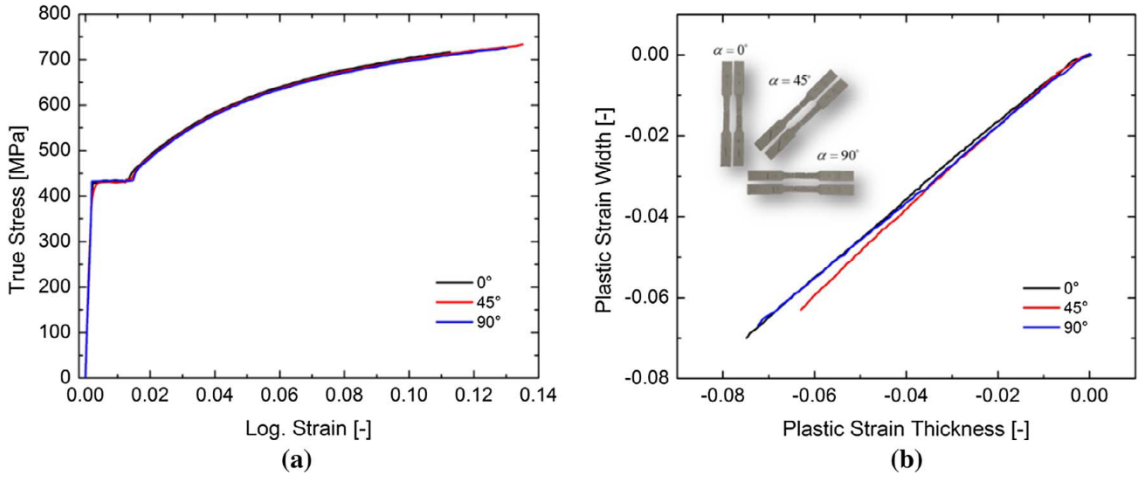

Fig. 2. (a) Engineering stress-strain curve at room temperature of TC128 uniaxial tensile test at three material orientations and its repetitions; (b) Plastic strain width to thickness curves for transverse (90°), diagonal (45°) and longitudinal (0°) directions. The slope of such curves represent the amount of anisotropy (Lankford ratio).

3. Constitutive modeling

3.1. Plasticity equations

In the present study, however, the material will be treated as isotropic whose yielding condition is described accurately by J_2 flow theory of plasticity (quadratic yield function) along with the associated flow rule in the form

$$f(\sigma,\bar{\varepsilon}_p) = \bar{\sigma}_{vM} - k = 0 \tag{1}$$

where $\bar{\sigma}_{vM}$ is the equivalent stress and $\bar{\varepsilon}_p$ is the corresponding work-conjugate equivalent plastic strain. The deformation resistance k (yield stress) is defined through the hardening law

$$dk = H(\bar{\varepsilon}_p)d\bar{\varepsilon}_p \tag{2}$$

The evaluation of the present experimental data revealed that the combined Swift-Voce law through a weighting factor (α) provides a very good approximation to the flow curve of TC128 in the post-necking stage, given by the following expression [56–58]

$$k = \alpha[A(\bar{\varepsilon}_0 + \bar{\varepsilon}_p)^n] + (1-\alpha)[K_0 + Q(1-e^{-\beta\bar{\varepsilon}_p})] \tag{3}$$

where A, $\bar{\varepsilon}_0$ and n are material constants of Swift equation; and K_0, Q and β corresponds to Voce equation. Note that the quadratic yield function is assumed for the simulation of the global response.

3.1.1. Parameters identification

The parameters needed for plastic flow calibration including post-necking behavior follows a hybrid numerical-experimental procedure, where finite element simulations match with measured load-displacement response by changing a weighting coefficient iteratively of a given geometry [59]. Eq. (3) outlines a combined Swift-Voce plastic flow evolution with three parameters for each type yielding a total of six parameters needed to be calibrated. Uniaxial tensile test provides enough information to determine those magnitudes by fitting the experimental true stress-plastic strain response until the onset of necking. The weighting coefficient α is adjusted iteratively by matching load-displacement curve from simulations with measured data of a selected geometry. Ideally, double edge circular cutouts flat specimens (NT20) are used for such purpose since diffuse necking and localization occurs almost in the same place (narrow band centered in the specimen between circular notches) guaranteeing repeatability. For instance, black solid line indicates the optimized fitting parameter $\alpha = 0.6$, while the colored lines display the power law (Swift) and saturate-type (Voce) hardening curves with $\alpha = 1$ and $\alpha = 0$, respectively as shown in Fig. 3a along with the measured load-displacement response (open circles). The calibration process is then completed by using only two distinct geometries (UT and NT20) to define pre and post-necking parameters as detailed in Table 2. All the remaining simulations in Fig. 3 can be deemed as validation, which proves the robustness of the present constitutive modeling. The selected geometries for material characterization includes double circular cutouts tensile flat specimens with different radii (NT20 and NT6.67), central hole with 8 mm diameter (CH8), special shear-design butterfly specimen (BF) and circular mini punch disk (PU) [59–61]. Likewise, notch round bar specimens with 2.0 and 1.0 mm radius for high triaxiality levels were employed [62]. Details of specimen dimensions and experimental procedure are not given here, but for interested readers are referred to the work of Paredes et al. [55].

3.2. Fracture equations

Under an uncoupled phenomenological approach, damage indicator can be expressed as a weighted von Mises equivalent plastic strain

$$D = \int_0^{\bar{\varepsilon}_p} \xi(\sigma)d\bar{\varepsilon}_p \tag{4}$$

where $\xi(\sigma)$ is considered an isotropic weighting function of the Cauchy stress tensor. Assuming a proportional loading path, the damage indicator predicts fracture initiation once reaches unity. On the other hand, a non-proportional increment of stresses leads to a faster damage accumulation, which tends to underpredict the onset of fracture and subsequent crack propagation [63,64]. The Mohr-Coulomb (MMC) fracture criterion [54] is considered as a weighting function in the present study, in which the limit of ductility is defined by a three dimensional mixed space of equivalent plastic strain ($\bar{\varepsilon}_p$), stress triaxiality (η) and Lode angle ($\bar{\theta}$) in the form

$$\xi(\sigma) = \left\{\frac{A}{C_2}\left[C_3 + \frac{\sqrt{3}}{2-\sqrt{3}}(1-C_3)\left(\sec\left(\frac{\bar{\theta}\pi}{6}\right)-1\right)\right]\left[\sqrt{\frac{1+C_1^2}{3}}\cos\left(\frac{\bar{\theta}\pi}{6}\right) + C_1\left(\eta + \frac{1}{3}\sin\left(\frac{\bar{\theta}\pi}{6}\right)\right)\right]\right\}^{\frac{1}{n}} \tag{5}$$

where η and $\bar{\theta}$ are invariants of the Cauchy stress tensor and are defined as follows

$$\eta = \frac{\sigma_m}{\bar{\sigma}} \tag{6}$$

where σ_m is the mean stress and $\bar{\sigma}$ is the equivalent von Mises stress. The normalized Lode angle $\bar{\theta}$ is expressed by

$$\bar{\theta} = 1 - \frac{2}{\pi}\cos^{-1}\left(\frac{r}{\bar{\sigma}}\right)^3 \tag{7}$$

where r is the third invariant of the deviatoric stress tensor given by

$$r = \left(\frac{9}{2}\underline{S}\cdot\underline{S}:\underline{S}\right)^{1/3} \tag{8}$$

[S] is the deviatoric stress tensor. The model parameters c_1, c_2 and c_3 are material constants. This particular three-parameter weighting function is used as it can be easily fitted to experimental data covering a wide range of stress states. Following the recommendation of Bai and Wierzbicki [54], the hardening exponent n is determined from the fitting of the stress-strain curve through Swift law (see Table 2). Likewise, Paredes et al. [55] described step-by-step procedure to adjust strain softening parameters for ductile crack propagation, which is adopted herein to complete the fracture process. Upon fracture initiation, stresses are progressively reduce until the total loss of the load carrying capacity of element is attained. A functional relation between damaged and undamaged equivalent stress is then defined [65]

$$\tilde{\sigma}_{flow} = \varpi\bar{\sigma}_{flow} \tag{9}$$

where $\tilde{\sigma}_{flow}$ is the softened flow tensile strength, $\bar{\sigma}_{flow}$ is the original flow tensile strength of the undamaged continuum with no softening. The softening coefficient ϖ follows a non-linear power-law evolution

$$\varpi = \left(\frac{D_c - D}{D_c - D_0}\right)^m \tag{10}$$

where D_c, D_0 and m corresponds to the critical damage, damage initation and softening exponent, respectively. Here, fracture initiation begins when $D = D_0 = 1$ in the material point (gauss point) and increases incrementally under straining (like the growth of an idealized internal crack) until critical damage is reached $D = D_c$, thus eroding the finite element from the mesh. Fig. 4 displays some of the possible paths that softening might follow based on m exponent selection.

The required work to relief the plastic strain energy accumulated in the element might be supplied either by gradually release of elastic strain energy in the neighboring elements or by controlled displacement. This process takes place in the range of $1 < D < D_c$, while the element is progressively losing its load carrying capacity. Therefore, the softening parameter ϖ can be viewed as a rate controlled parameter for crack propagation, where D_c and m defines the amount of additional

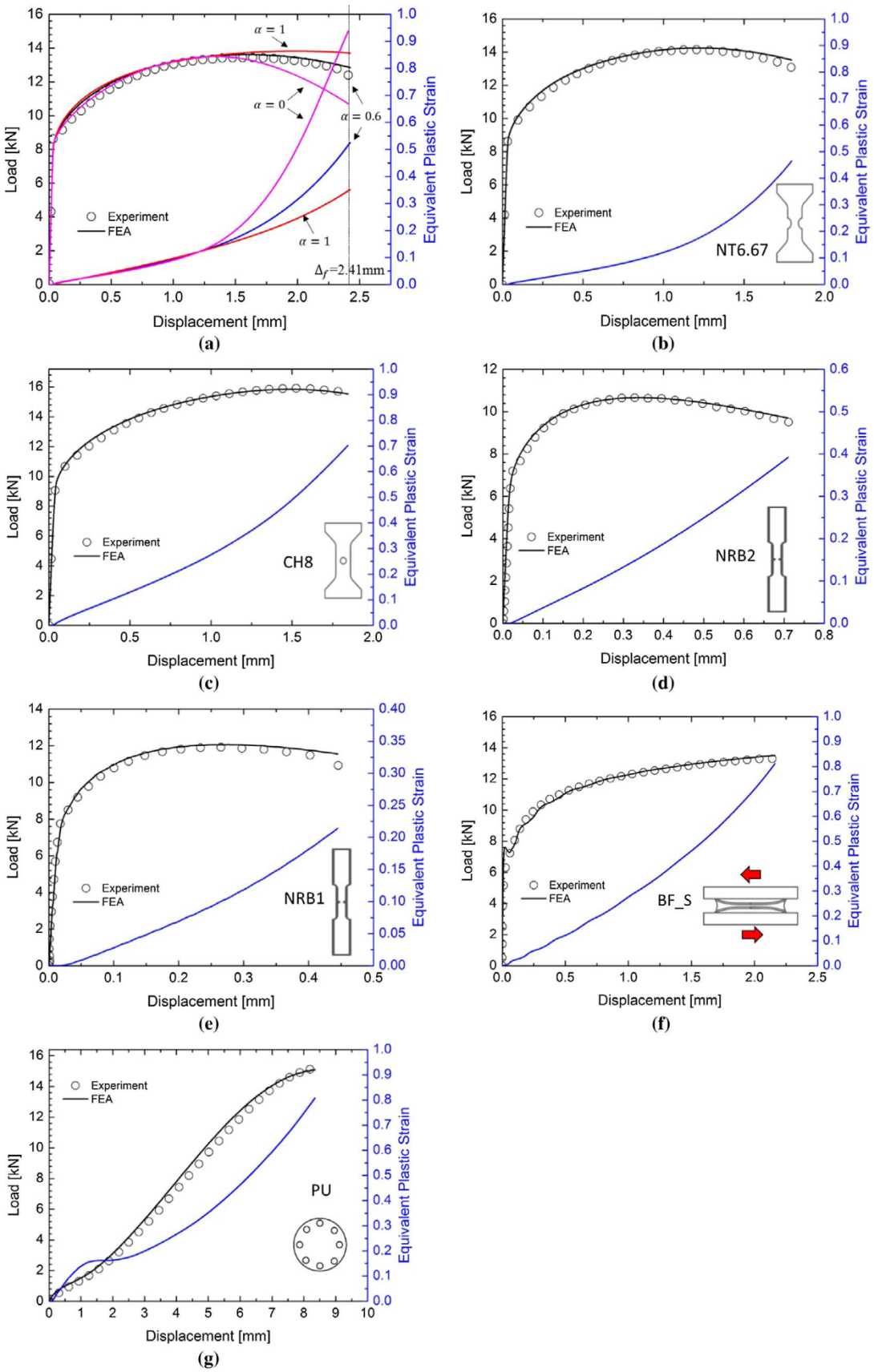

Fig. 3. Force-displacement curves for material characterization of TC128 steel: (a) NT20; (b) NT6.67; (c) CH8; (d) NRB 1.0; (e) NRB 2.0; (f). BF Shear and (g) Punch specimens. The solid lines represent numerical simulations while open symbols indicate experimental results.

Table 2
Plasticity and fracture parameters for TC128 tank car steel.

Plasticity parameters							Fracture parameters		
Swift			Voce				MMC		
[MPa]	[–]	[–]	[MPa]	[MPa]	[–]	[–]	[–]	MPa	[–]
A	ε_0	n	K_0	Q	β	α	c_1	c_2	c_3
1105.7	0.005	0.2	393.4	373.8	18.5	0.6	0.165	620.5	0.969

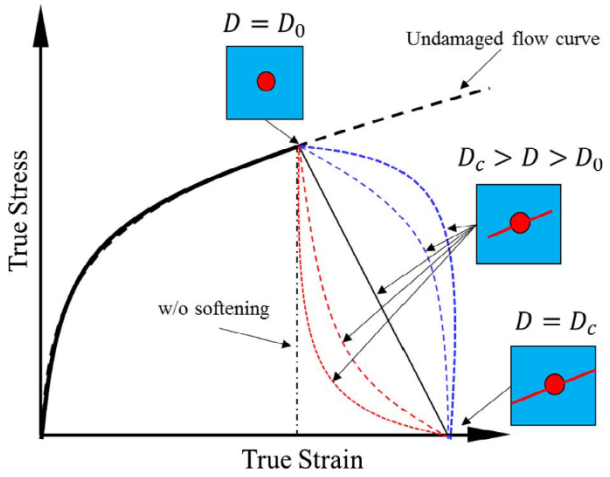

Fig. 4. Post-failure softening technique at different m exponent values: $m > 1$ (colored red dash lines); $m < 1$ (colored blue dash lines) and $m = 1$ (colored black solid line). (For interpretation of the references to colour in this figure legend, the reader is referred to the web version of this article.)

damage required to extinct the element. For $m \neq 1$ the softening function (ϖ) follows a power law trend which accelerates ($m > 1$) or delay ($m < 1$) the stress reduction while $m = 1$ leads to a linear energy dissipation.

3.2.1. Parameter identification

Fracture initiation is assumed to occur when the load from the load-displacement curve drops sharply. This fracture point is represented as the end of the measured load-displacement curve (open circles) in Fig. 3. Additionally, the evolution of equivalent plastic strain, extracted from the critical element, with respect to displacement is also included to facilitate the interpretation of the inverse method, herein performed, to characterize the limit of ductility. In Fig. 5 the loading history in terms of the normalized stress invariants (η,$\bar{\theta}$) and equivalent plastic strain ($\bar{\varepsilon}_p$) are plotted for all samples considered in this study. Nearly plane stress condition is observed in most of the flat specimens, since fracture initiation points lie over the plane stress curve (blue solid line) [66]. On the other hand, stress triaxiality concentration is intense in the center of notched round bars, which leads to a premature fracture initiation and thus lower plastic strain. The three free-parameters c_1, c_2 and c_3 are calculated numerically by matching fracture initiation points with those obtained from experiments. As a result, the fitted fracture parameters for initiation, detailed in Table 2, yields predictions (open triangles) which are in good agreement with the measured loading history extracted from simulation. The end of each solid line corresponds to the point of fracture initiation in experiments.

3.2.2. Fractography of fractured surface

Fig.6 depicts the fracture surface of two notched round bar specimens subjected to tension. The severity in radial contraction is more evident for large radius than for small one due to presence of necking. Plastic instability in the gage section tends to reduce gradually the net cross section area, elongating toward transverse direction as shown in Fig. 6a. This mild anisotropy is captured by the measure of the Lankford coefficients (see Section 2), which can be treated, in this case, as isotropic for modeling purposes. Meanwhile, little contraction is observed in the configuration with small radius, since notch acuity removes coupling between fracture and plastic localization at the gage length. The circular cross section remains almost unchangeable under plastic deformation producing the well-known “cup and cone” fracture morphology. A large concentration of dimples is observed over the surfaces, being more prominent in the center where the stress triaxiality is high and the void growth mechanism controls the fracture process mostly. This is also an indicative of the degree of impurity present in the material, which in turn leads to a significant diminishing of its ductility. On the other hand, plastic strain controlled regions are more visible in the periphery of the specimen near to the notch root generating slant fracture morphology.

At the microstructural level, the nucleating particles trigger the cavities formation within the material when loaded plastically. In this case, second phase particles, presumably, MnS or CaS particles nucleate first into voids for being the larger inclusions present in the matrix (~50 μm). As deformation increases, secondary particles (carbides or M-A constituents ~ 2 μm) contributes to the growing of the void by nucleating at lower stress triaxiality level but higher plastic strain concentration. Eventually, the system coalesce by instability of internal ligament between voids generating dimples as shown in Fig. 7. In regions where triaxiality is intense, cavities tend to be larger compared to cavities formed in the periphery. For instance, coalesced voids size in the center are in average ~30–40 times larger the size of voids in the notch root. Additionally, despite similarity between dimples configuration in both specimens (Fig. 7a and b), small notch radius specimens yield higher stress triaxiality levels at midplane and thus the coalesced particles would be expected to be wider than others developed in less acute notched bars.

In general, typical rounded dimples with well form lips/rims are observed on the surface. The SEM image suggest that the nucleation sites are widely spaced, allowing for free volumetric expansion and thus the microvoids grow to a large size before coalescing with neighboring voids, resulting in large dimples formation [11,12].

4. Tearing analysis

In the subsequent section, the calibration of the strain softening parameters are conducted. An ad-hoc procedure outlined by Paredes et al. [55] is followed to adjust crack propagation parameters by matching the resistance curve of a selected specimen geometry and then validating in a different configuration. In particular, three-point single edge notch SE(B) and compact tension C(T) specimens were selected for calibration and validation, respectively. Fig. 6 shows the geometries with their respective dimensions and shapes. For simplicity the specimen thickness was kept constant for both specimens (18 mm), the machined pre-crack was set 4 mm for SE(B) and 31.3 mm for C(T), see details in Fig. 8. The SE(B) has a square cross-section area with optional integral-machined knife edges of 1.4 mm depth for single-cantilever clip-in displacement gage. A span length between supports was four times the width as established by the standard procedure ASTM E1820-13 [67].

4.1. Experiments

4.1.1. Single edge notch bending test

Three SE(B) specimens were extracted along the longitudinal axis (0°) from the circular plate for ductile resistance assessment. ASTM E1820-13 [67] suggests the samples should be prepared out the material core by eliminating outer and inner layers but keeping the width to thickness ration between one and four $\left(1 \leqslant \frac{W}{B} \leqslant 4\right)$. However, the actual thickness samples is much less than the wall-thickness of the plate,

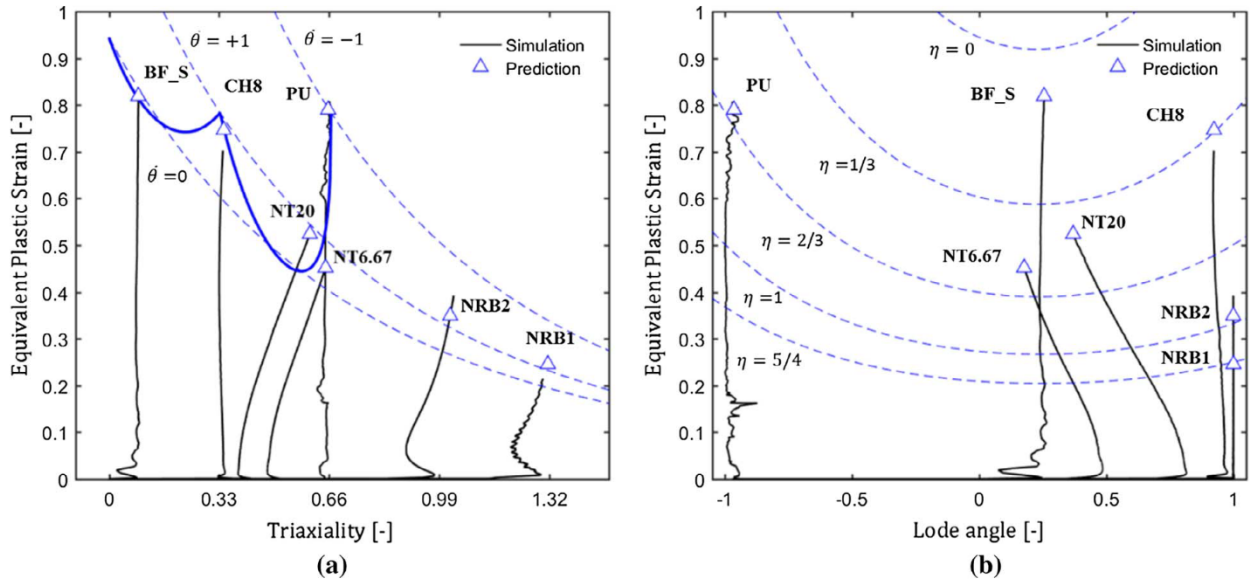

Fig. 5. State of stress for seven different specimen geometries in the mixed strain to fracture space in terms of: (a) stress triaxiality and (b) the Lode angle parameter. While the open symbols represent the fracture initiation points predicted by the model, the measured strain to fracture is indicated by the end of solid lines.

but it is believed such difference would not affect the final results. The specimen and crack plane location follows typical L-S orientation (Y-X) with initial crack size of $a = 4$ mm, width $W = 18$ mm and $B = 18$ mm. These dimensions yield the following ratios: $a/W = 0.22$, $W/B = 1$. Moreover, to guarantee acceptable constrain levels at the crack-tip, the norm recommends a span between roller pins to width ratio, $S/W = 4$. The fatigue pre-cracks were introduced using three point (3P) bending device at high frequency but short amplitude (more easily than tensile force). After fatigue pre-cracking, the final crack extension reached $a_0 = 5$ mm ($a_0/W = 0.28$) and then v-shaped side grooves were machined at both sides of the specimen to promote uniform crack growth. The side-groove depth was 7.5% on each side giving a net specimen thickness (B_N) equal to $0.85B$. The side-grooves were machined according to the ASTM E1820 standard requirements [67], that is root radius in the range of 0.5 ± 0.2 mm and angle less than 90°. One SE(B) specimen was tested using a single clip gage device attached to the outer specimen surface to measure the crack mouth opening displacement (CMOD). The remaining two SE(B) specimens were tested using two clip gages using special knife device to record displacements at two different positions from the specimen surface. Having two displacements above the crack mouth is straightforward to obtain the crack tip opening displacement CTOD (δ) by simple trigonometric relations. This procedure is known as Double Clip Gage (DCG) method and is routinely used by the oil and gas industry to measure the fracture toughness of pipeline steels. For further details of the DCG the reader is referred to previous works [68,69]. The CTOD (δ) can be inferred by the following expression as well:

$$\delta_i = \frac{J_i}{m\sigma_y} \tag{11}$$

where J_i is the i-th energy release rate measured by the compliance method to determine J resistance curve, m is a plastic factor correction and σ_y is the yield stress. Previous parameters are directly computed from the measured load-CMOD curve using the compliance method and the continuous average crack extension given by the testing protocol ASTM E1820-13 (see illustrative examples about the relation $J - \delta$ [86,87]). The norm states that the maximum recommended range of unload/reload for crack extension measurement should not exceed either 50% of Pm (max load) or 50% of the current force, whichever is smaller. Fig. 9 shows the results of experimental measurements of the load-CMOD and CTOD resistance curves for several loading/unloading stages. As can be seen in Fig. 7b the fracture toughness curves obtained from Eq. (11) (ASTM 1820-13) and DCG are in good agreement for $\Delta a > 0.5$ mm. This outcome proves the existing connection between J and CTOD with the physical measure of the crack-tip opening by means of DCG device for stable ductile crack propagation. However, initial crack growth stage due to blunting is not well captured by neither of the aforementioned procedures, since the change of elastic compliance

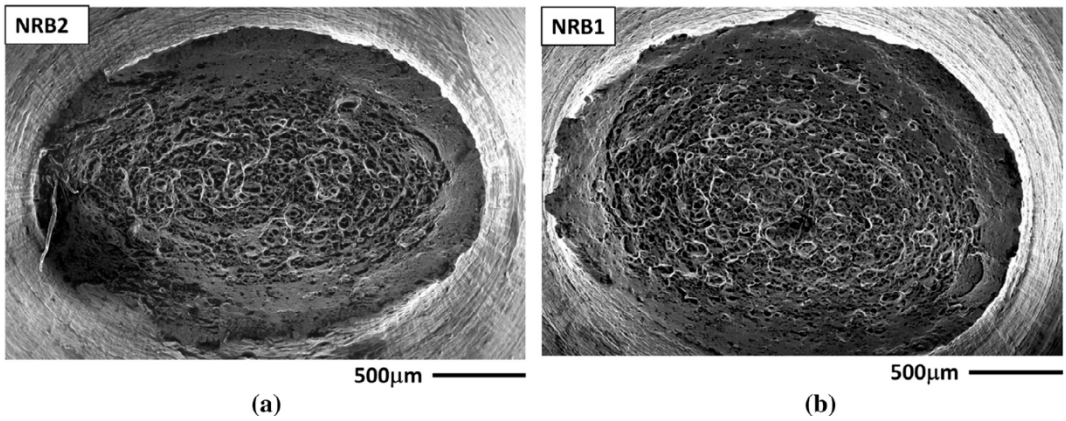

Fig. 6. Scanning electron microscope (SEM) images of notched round bars with different radii: (a) 2 mm and (b) 1 mm.

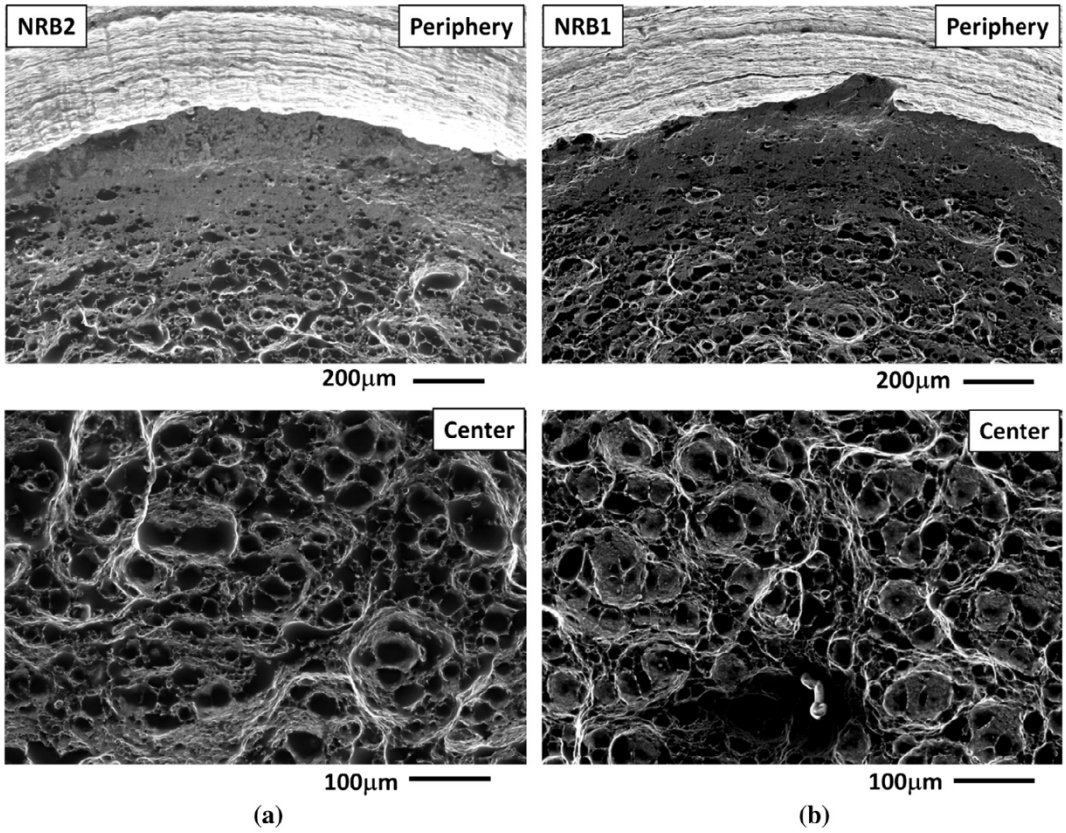

Fig. 7. Amplification of fracture surfaces of notched tensile bars with 2 mm (left column) and 1 mm (right column) from center and periphery (root).

during this stage is not necessarily related to the creation of new fracture surfaces [55]. Thus, measurement of the exact instant of the onset of ductile crack extension is not possible and scatter can be observed before $\Delta a \sim 0.5$ mm, where the specimen responses exhibit an apparent negative crack growth. This is a well-known problem during fracture testing of SE(B) specimens. Similar experimental behavior has been reported in the open literature. Different explanations have been given: friction, misalignment, specimen rotation, residual stresses during unloading, analysis method, localized deformation, etc. The precise causes of this phenomenon are not fully understood and further studies are needed.

4.1.2. Compact tension test

Constraint has been studied exhaustively to understand its effect on fracture toughness values [38,70–72]. Cracked components having high restriction to plastic deformation reduces its ability to support external load when compared to cracked structures with low restriction to plastic deformation. Thus, the fracture toughness of specimens (structural components) can varies dramatically as function of the constraint. The previous SE(B) specimens with shallow cracks possess low constraint level, then the CTOD-Δa curves shown in Fig. 9b can be considered as high resistance fracture toughness values for the TC128 steel. To test the capability and robustness of the MMC model in predicting

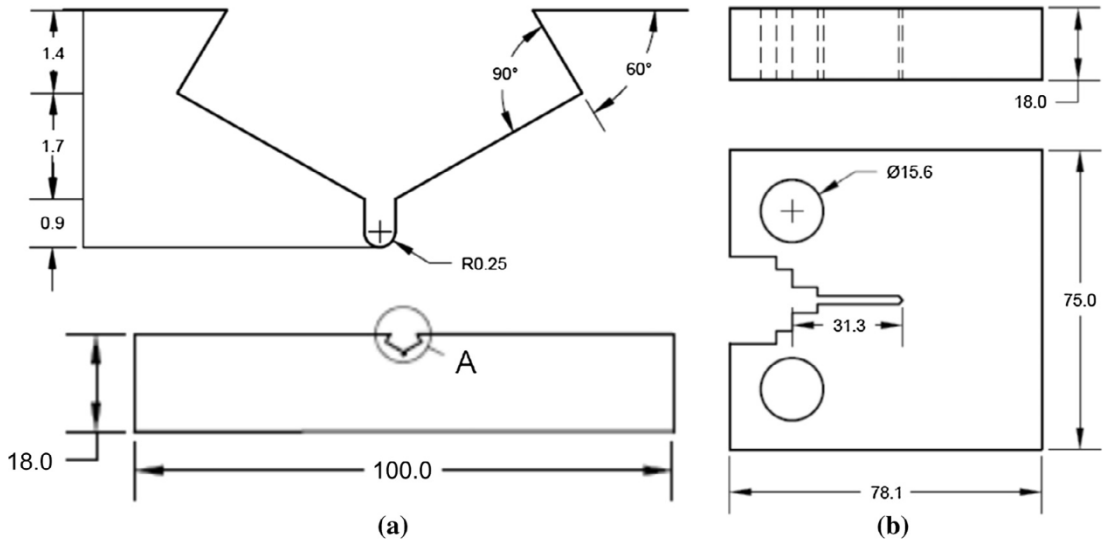

Fig. 8. Standard fracture mechanics specimens: (a) Three-point bending single edge notch SE(B) and (b) Compact tension C(T).

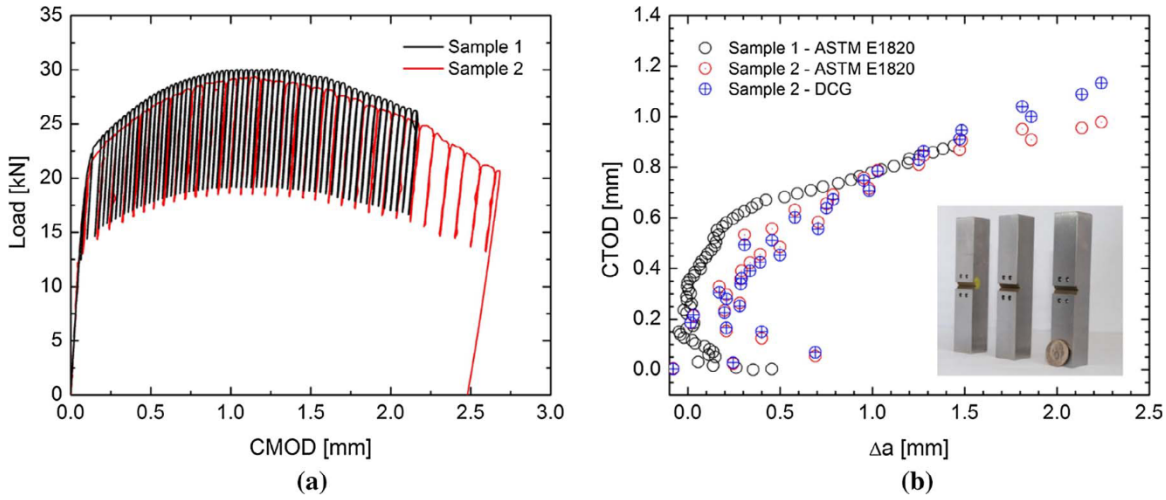

Fig. 9. Experimental fracture response of SE(B): (a) Load-CMOD curve and (b) CTOD resistance curve.

crack extension, a high constrained compact tension C(T) specimens was chosen to be tested during the experimental campaign. In particular, C(T) is employed to perform a validation study on crack growth response. The resistance curves were obtained from three nominally identical specimens having deep crack size ratios, $a/W = 0.5$, with $W = 62.5$ mm and $B = 18$ mm. Fracture toughness as well as ductile tearing was measured by the testing procedure outlined in the ASTM E1820 standard for the C(T) specimens. It is necessary to correct the specimen compliance, C, in order to take into account the changes in specimen position due to specimen rotation as the test progresses. Specimen rotation shifts the measurement points for the applied load and CMOD with reference to the original (undeformed) configuration upon which the specimen compliance C is based on. At the maximum CMOD value the correction on fracture toughness and crack length were up to 20% and 10% respectively. Likewise, v-shaped side grooves were machined to promote uniform crack extension on C(T) specimens. For sample 1 the side-groove depth was 7.5% on each side giving a net specimen thickness (B_N) equal to 0.85B. For samples 2 and 3 the side-groove depth was 10% on each side giving a net specimen thickness (B_N) equal to 0.80B. *All* side-grooves were machined according to the ASTM E1820 standard recommendations.

The resistance curves obtained for both C(T) configurations are shown in Fig. 10b. It can be seen that sample 2 and 3 produce similar remote and local behavior in terms of Load-CMOD and CTOD-Δa resistance curves. Meanwhile, R-curve and Load-CMOD responses for sample 1 are higher than the previous two specimens (samples 2 and 3). The post-mortem crack front measurement reveals that the initial crack length of sample 1 was 1 mm shorter than samples 2 and 3. This fact along with the increasing net specimen thickness (due to reduced groove size) leads to a higher response.

4.2. FE models

Finite element modeling of SE(B) and C(T) requires more attention, especially, in crack-tip details and side groove sides. As before, taking advantage of its symmetry, only a quarter of the complete sample is built with the corresponding symmetry conditions to insure continuity. Fig. 11a shows a shallow-cracked SE(B) specimen with $a_0/t = 0.28$ (after pre-cracking), $W = 18$ mm ($W/B = 1$) and $S/W = 4$. The crack front is composed by a set of isoparametric elements uniformly distributed from the symmetry plane toward free surface, even for the remaining crack plane. As before, 8-node trilinear solid element (C3D8R) is used with a dimension of 200 × 200 × 200 μm. The element size is similar to the one used for calibration process in order to remove possible mesh size effect. The quarter-symmetric model has around ≈ 48,000 8-node and ≈60,000 nodes arranged into several constant thickness layers over the half-thickness of the model. A circular cutout was introduced at the free surface of the model with a root radius of 0.60 mm and offset groove angle of 60°. The 10% side groove (S.G.) is built above the first layer forming the crack plane. This is done to avoid

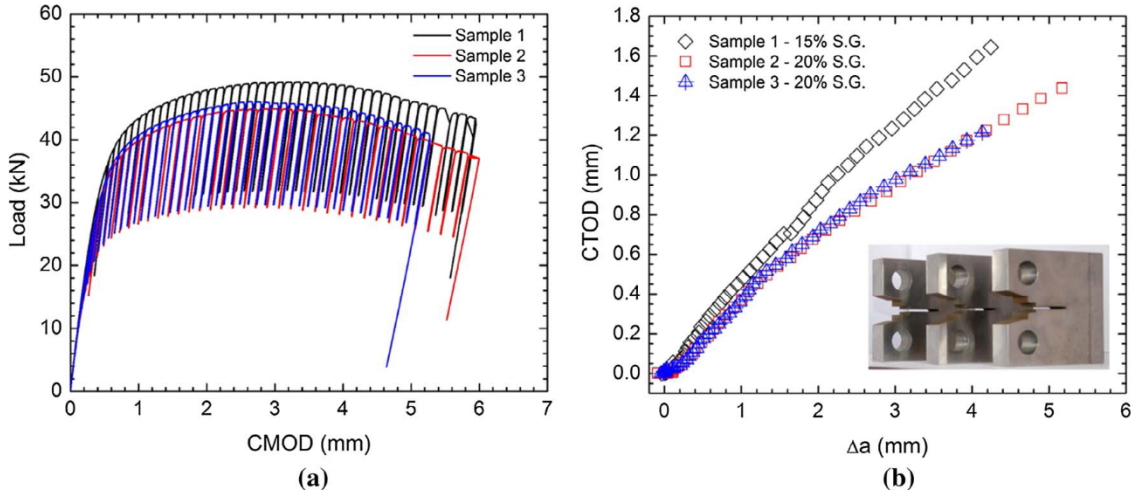

Fig. 10. Experimental fracture response of C(T): (a) Load-CMOD curve and (b) CTOD resistance curve.

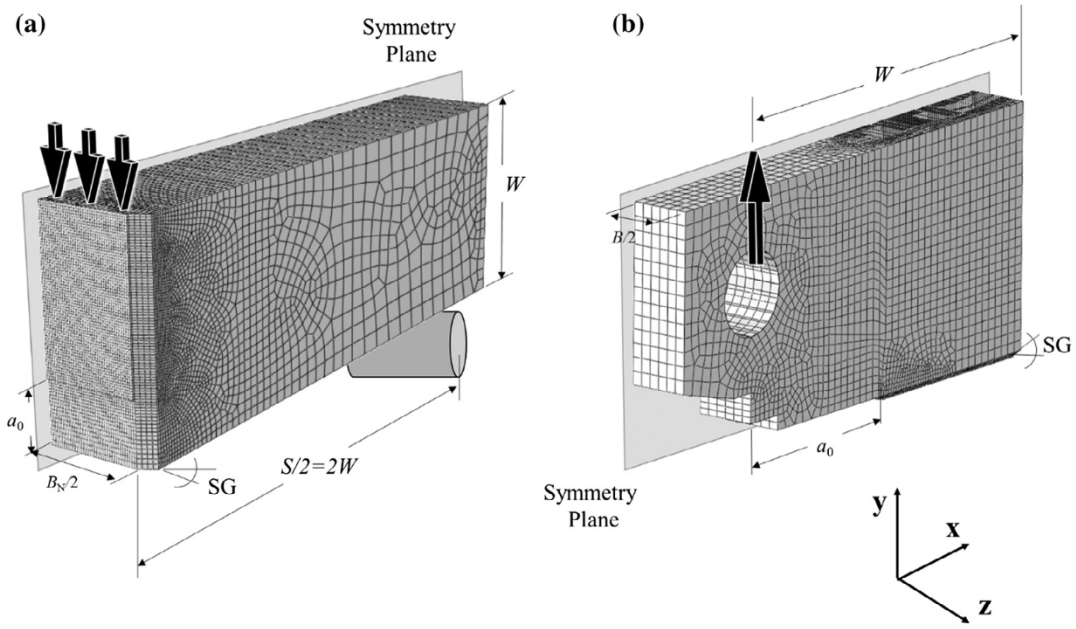

Fig. 11. Three-dimensional FE models for (a) SE(B) and (b) C(T).

excessive plastic deformation, which in turn will lead to a non-realistic crack propagation along the side grooved side. The CTOD value was extracted from a fixed node in the symmetry plane located at one node above the crack-tip node. In particular, the developed plastic deformation around the crack-tip is well captured during the loading in that position [55]. The computed fracture resistance curve is based on the instantaneous CTOD quantity computed as described above. The crack front is not straight and the average crack growth is defined as the swept area by deleted elements forming the growing crack front divided by the specimen thickness. For blunting stage, no element is removed from the mesh and the finite slope describing the blunting evolution in the resistance curve corresponds to the average nodal displacements of the crack front nodes in the propagation direction. This stage ends when the first element is extinguished and the crack advances creating new fracture surfaces.

The numerical analyses carried out in this investigation was using Abaqus/Explicit software package [73]. The explicit solvers use a central difference time integration scheme with 2nd order accuracy, which is only conditionally stable. Further, the ABAQUS/Explicit has the capability to incorporate the failure criterion used in conjunction with J_2 plastic flow through user-defined subroutine VUMAT. The code enables the element removal once they reached a critical value, then setting all stresses to zero. Subsequently, the incrementally element removal describes ductile crack growth.

4.3. Crack growth resistance

After post-mortem examination on the fracture surface morphology of the specimens, it was found that SE(B) exhibits a more uniform crack propagation through thickness than C(T) specimens as shown in Fig. 10. In particular, SE(B) is internally subjected to a combined tension-compression loading mode along the remaining ligament, being opening stresses at the crack-tip side and compressive forces at the loading point. This stress constraint along with the side grooves leads to a uniform ductile tearing response almost all the way of crack propagation, which differs strongly with C(T) fracture surface morphology due to tensile dominating condition and lower B/W ratio. The latter exhibits two advancing crack fronts: one in the center and other in the edges as shown in Fig. 12b, which gives rise an uneven crack extension through the remaining ligament. In engineering critical procedures, the average of crack growth is used to construct the fracture resistance curve defined in terms of CTOD. The purpose of side grooves in specimens is just to promote an even moving crack front as grows, thus reducing the variance of its mean value. On the light of this evidence, the SE(B) specimen becomes ideal for calibration procedure and C(T) for validation.

Paredes et al. [55] outlined an experimental/numerical procedure to calibrate and validate crack propagation response of standard fracture mechanics specimens. Herein, such procedure is followed. An iterative process to find softening parameters is implemented by minimizing a cost (objective) function

$$\mathrm{Min}(Error) = \left(1-\frac{P^{num}}{P^{exp}}\right)^2 + \left(1-\frac{\delta^{num}}{\delta^{exp}}\right)^2 \tag{12}$$

where the superscripts *num* and exp represent the numerical and experimental measures of load P and CTOD δ, respectively. A graphical representation of this scheme is depicted in Fig. 13. The black solid line represents the model without softening option, which indicates the premature fracture propagation trend by decreasing the load response as crack mouth opening increases. This behavior is reflected locally by a lower fracture resistance curve as depicted in Fig. 13b. On the other hand, by application of Eq. (12) a suitable set of softening parameters can be obtained by systematically minimization of the error derived from differences between experiments and simulations. The final adjusted parameters for post-initiation softening are: $D_c = 1.8$ and $m = 0.1$; and it is represented by red solid line in global Load vs. CMOD curve and local CTOD resistance curve as shown below.

Once the set of parameters are ready not only for initiation but also for crack propagation a validation study is conducted on C(T) specimens. In Fig. 14 are depicted the fracture response of such specimens globally and locally in function of Load-CMOD and CTOD-Δa. It is clear the existing transferability between specimen geometries subjected to the same type of loading mode, which proves the self-similarity of fracture process. In the same manner, this may be evident when comparing fracture morphologies between FE simulations with experimental observations.

4.4. State of stresses in the crack front

Crack-tip conditions defines how the crack will propagate along the remaining ligament. Despite the evident strong strain gradients along the crack front, the stress distribution along remaining ligament plays

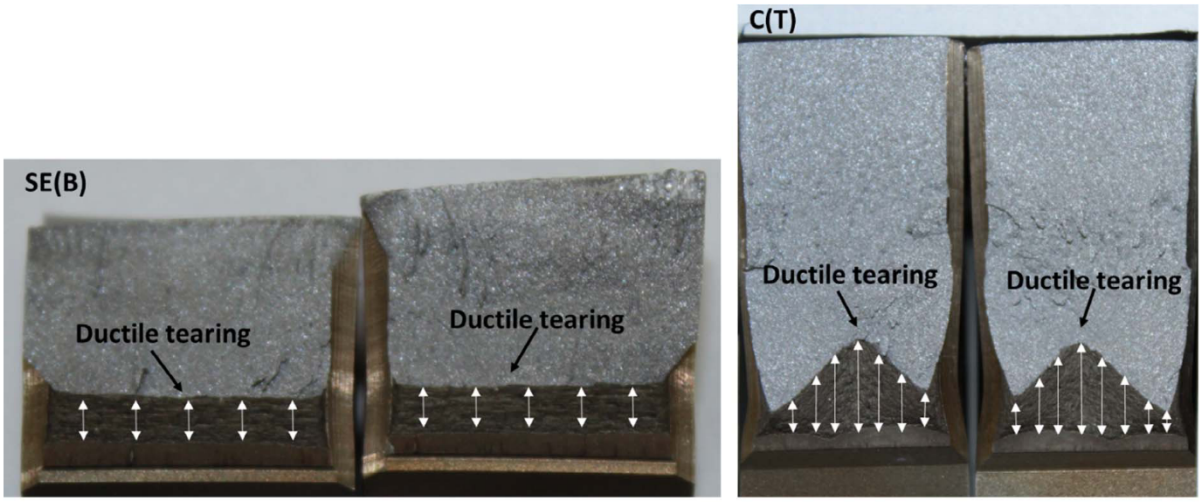

Fig. 12. Fracture morphology of specimen surfaces after experiments: (a) SE(B); (b) C(T).

an important role in fracture crack propagation. Consider now snapshots of the state of stresses of a growing crack for both geometries at certain level of deformation as depicted in Fig. 13, where equivalent plastic strain, stress triaxiality and normalized Lode angle are spatially represented by the position r of the material in the undeformed configuration for material points lying along the crack line ahead of the tip. In order to scale down the spatial distribution of the state variables for different specimen types, the position r is normalized by $m\delta$ (see Eq. (11)). Thus, the length scale of the abscissa defines the position where the whole fracture process takes place. In the present analysis, fracture variables from two different locations were examined: symmetry plane and side groove root side (outer plane). The deformation level at which these snapshots were taken was the instant of initiation of stable crack propagation for the three configurations. The singularity zone characterized by intense plastic strain in the near-tip is higher for shallow crack SE(B) than for deep crack C(T) resulting in a pronounce blunting crack formation before propagation. The blunting crack element is subjected to biaxial loading since one of the in-plane stress component is zero (fracture plane) whereby relaxing the stress triaxiality within this zone ($r/(m\delta) \sim 1$). Despite having this special plane stress state evolving at the crack-tip in the symmetry plane, the surrounding material prevents the near-tip material from contraction producing the plane strain condition characterized by the third invariant (Lode angle). Under such condition, the Lode angle is zero, whereas is $+1$ and -1 for axisymmetric tension and axisymmetric compression, respectively as shown in Fig. 15c. The plastic zone at the center is presumably well contained for all cracked configurations since its extension is smaller relative to specimen thickness. Therefore, small scale yielding prevails and the single characterizing parameter concept (J or δ) is still applicable for fracture response. Meanwhile, the plastic zone along the side groove root extents largely 4–5 times the size of its alternative in the midplane. This plastic zone is comparable with specimen dimensions resulting in a severe stress relaxation denoted by the triaxiality in Fig. 15b, which remains almost constant along the crack direction ($r/(m\delta) > 1$). Along this region, the void growth mechanism is hindered by the absent of the out-of-plane stress component responsible to built-up the constraint level within the material at the crack-tip location. In turn, plastic strain controlled takes place making the crack runs faster than the crack in the center plane, e.g. see Fig. 17. The dominating loading condition at the free-surface crack-tip is almost plane stress having $\bar{\theta} \sim 0.9$–1 in the singularity zone. Although some exiting differences between specimen geometries, the stress state evolution follows similar pattern relative to each other. In particular C(T) configuration (for both side groove sizes) attains a lower peak stress ($\eta \sim 1.8$) in the zone where fracture process occurs ($r/(m\delta) \sim 1.5$) relative to SE (B) ($\eta \sim 2.5$). Deep crack fracture samples, usually, yield lower resistance curves in relation with their shallow cracked alternatives due to rapid crack propagation and small scale yielding around the tip. However, the

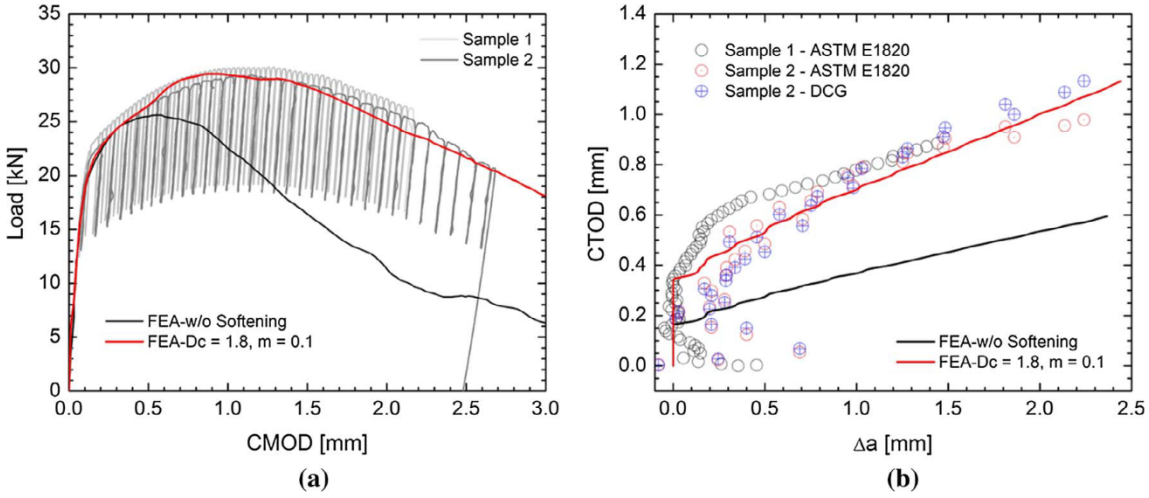

Fig. 13. Calibration of post-softening parameters using SE(B): (a) Load-CMOD curve and (b) CTOD resistance curve.

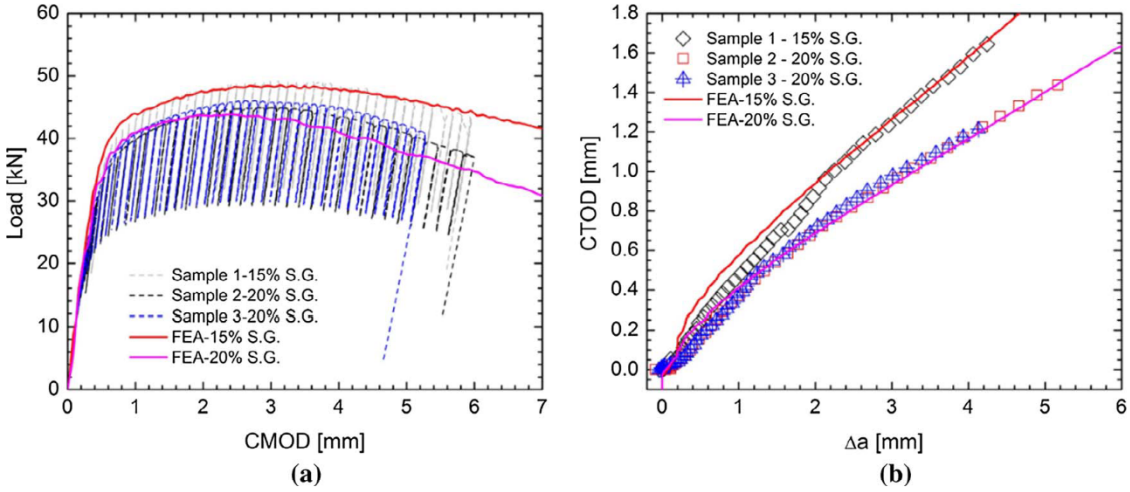

Fig. 14. Validation of model parameters through C(T): (a) Load-CMOD curve and (b) CTOD resistance curve.

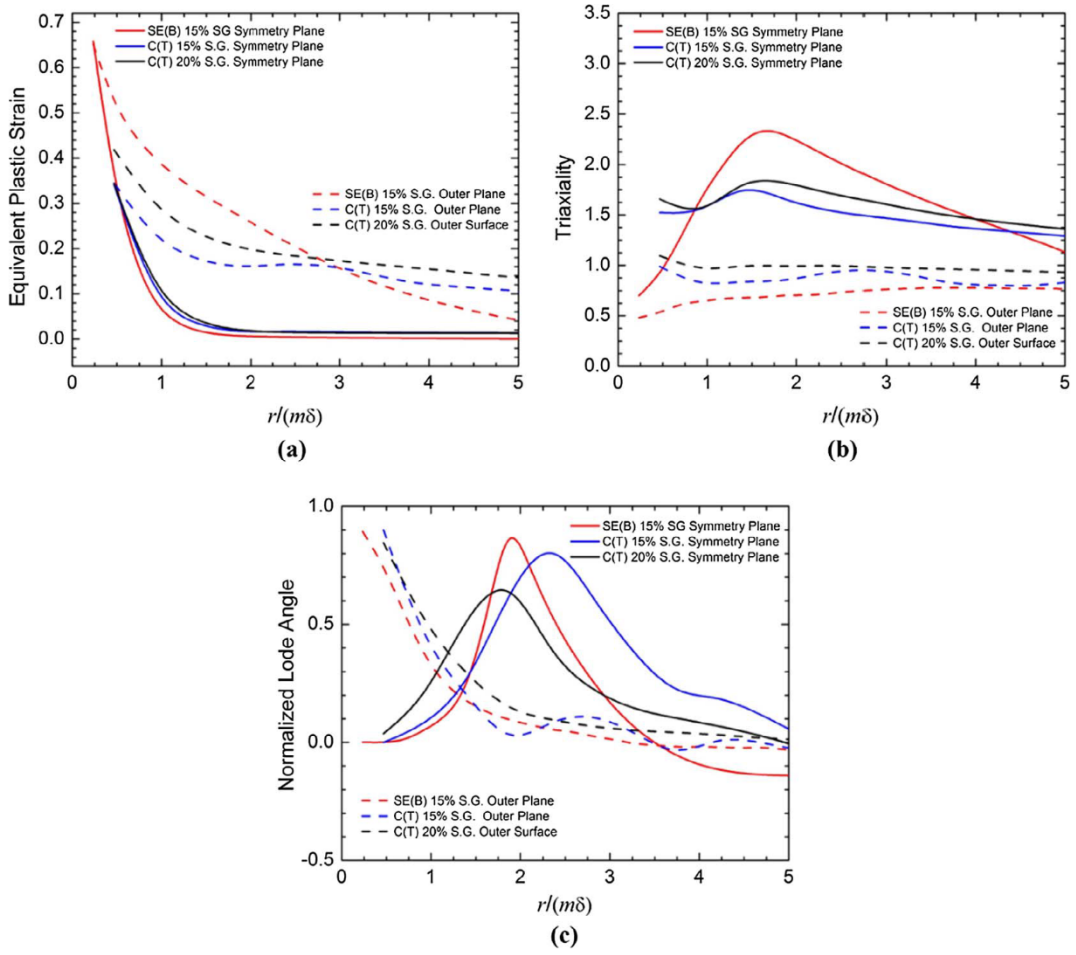

Fig. 15. State variables distribution on the plane ahead of the crack-tip (solid color lines) located in the symmetry plane and the crack-tip located in side groove root for C(T)'s and SE(B) at the instant of crack propagation.

side groove size tends to modify slightly the stress fields mainly in the fracture process zone, where axisymmetric tension ($\bar{\theta} \sim 0.8$) dominates the volumetric expansion of the void in actual fracture specimens.

The stress state distribution along the crack front is shown in Fig. 16. The transverse position S/B is normalize with respect specimen thickness (B) to scale down different net thickness due to side grooves. The distance at which the variables are extracted corresponds to region where the fracture process takes place ($r/(m\delta) \sim 1$) for three distinct deformation levels expressed in CTOD. The effect of side grooves on fracture propagation becomes important at early stages of loading by imposing intense plastic deformation fields in the side groove root. Thereby modifying the so-called thumbnail like tunneling crack front shape typically observed in C(T) samples. Meanwhile the stress triaxiality, as oppositely operator of equivalent plastic strain, attains its peak in the midplane (S/B = 0) and remains almost constant across the thickness until suddenly drops due to side groove presence (S/B ~ 0.9)

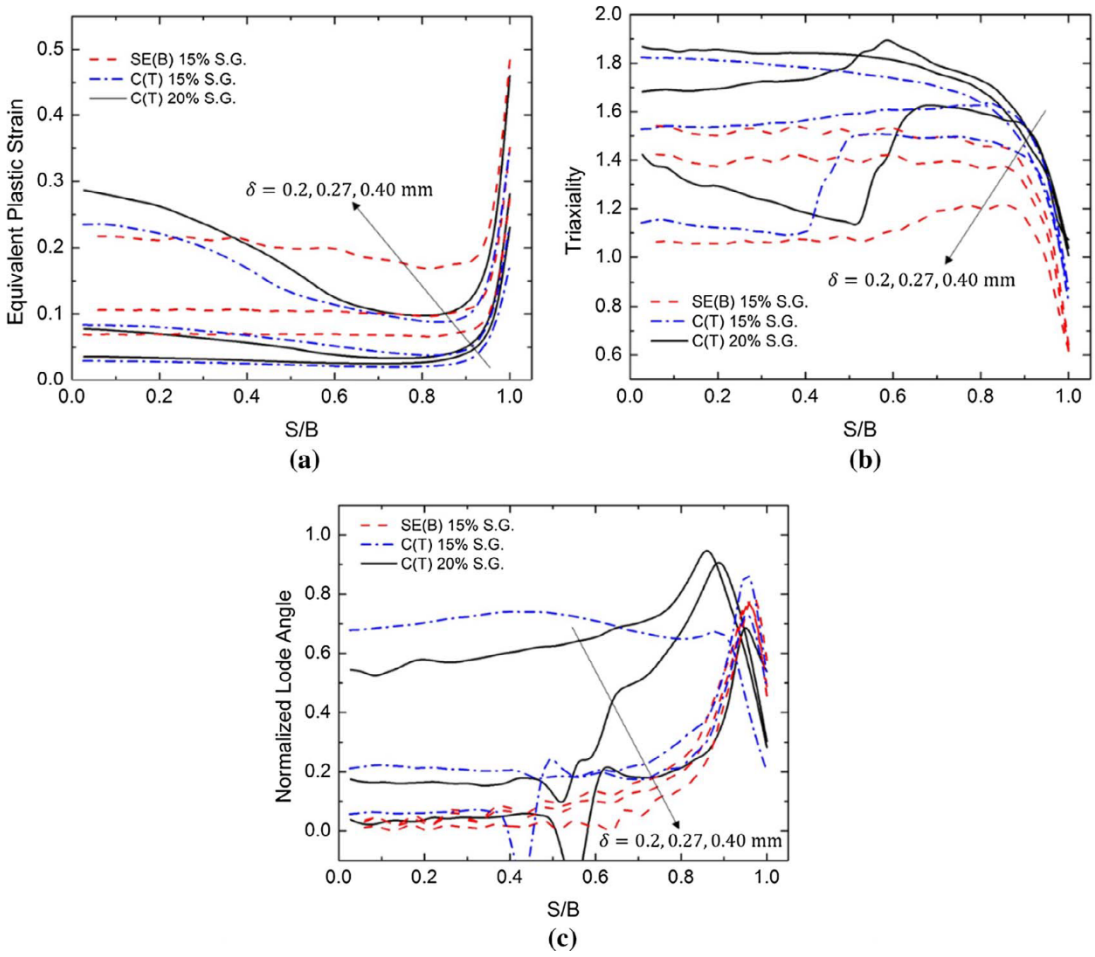

Fig. 16. Evolution of state of stress at the crack front for C(T) and SE(B) specimens including various levels of deformation in terms of crack-tip opening displacement (δ): (a) Equivalent plastic strain; (b) Stress Triaxiality and (c) Normalized Lode angle.

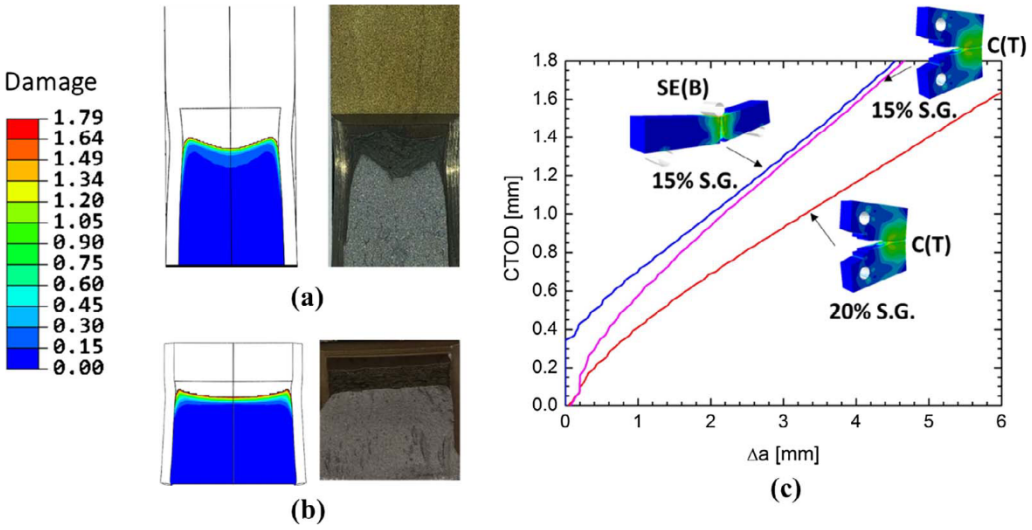

Fig. 17. Comparison of FE results with experimental observations of fracture morphology after test for: (a) C(T), (b) SE(B) and (c) *R*-curves (color coded scale corresponds to damage D_c). (For interpretation of the references to colour in this figure legend, the reader is referred to the web version of this article.)

e.g. see Fig. 16b. As deformation increases a second strain gradient field evolves in the center, accelerating the crack growing process, whose extension only covers 60% of the net thickness of the fracture plane as depicted in Fig. 16a. This characteristic fracture morphology is caused by the presence of the side grooves located on the specimen lateral sides to promote uniform growing crack fronts. In general this technique works when the B/W ratio is close to unity, as observed for SE(B) results, but fails for lower ratios resulting in the formation of a peak-valley crack front as displayed in Fig. 17. This uneven crack front is defined for having two highly concentrated localized zones (center and free-surface) and one with high triaxiality level in the neighboring of the side groove root. Moreover, SE(B) specimens display a completely distinct crack front shape as it advances as shown in Fig. 17. Due to comparable dimensions between width and thickness ($B/W = 1$), the side grooves work properly in promoting uniform crack propagation as evidenced by the state variables shown below. The strain gradient

through-thickness is almost constant as deformation increases except in the notch root, where the plastic strain spikes up. Likewise the triaxiality diminishes with increasing loading uniformly.

The Lode angle provides an important insight about the dominating loading state controlling fracture. In Fig. 16c the SE(B) geometry is mainly subjected to the state of plane strain as deformation increases with little effect on its history (red dash lines). Moreover, C(T) displays a more severe strain gradient, which in turn produce an intermediate state between axisymmetric tension and plane strain as deformation rises. When the elements participating in the fracture process are near to attain extinction, the dominating state becomes plane strain.

In Fig. 17 the simulated and experimental crack fronts along with the computed resistance curves are shown. The side grove effects is clearly evidenced by the presence of free-surface crack-tips as deformation increases. These cracks are characterized by developing low triaxialities but rapid speed propagation comparable to the rate growth of the central crack in the symmetry plane. For short crack extension ($\Delta a < 1$ mm) a faint thumbnail crack front shape develops with some shear lip trails around the side grooves. As crack grows in the center plane, lateral cracks tend to initiate and propagates as fast as it does leaving behind a sort of wake in between. This left-behind zone is defined by higher stress triaxiality and lower plastic strain (see Fig. 16a and b) and are responsible for the uneven shape of the growing crack front being more pronounced in C(T) than SE(B) as shown in Fig. 17a. On the other hand, the bending load in SE(B) yields a more uniform shape of the crack front as propagates, see Fig. 17b. This is opposed of what was observed by Mathias et al. [70] in similar dimensioned SE(B) specimen but made of different material (X80 steel). They found, after fracture surface examination, the crack front has propagated asymmetrically across the net thickness and a plausible explanation is an undesired misalignment between specimen and the testing assembly during fatigue pre-cracking. It is not clear if the mechanical properties (anisotropy or weld mismatch) have also had influenced on that process. In bending conditions for shallow cracks, the necking, which is preceded by area reduction, is meaningless compared to tensile loading mode, so crack extension due to blunting is inexistence and tearing occurs once the onset of stable crack growth is attained. In theory [72,78], initiation of ductile tearing is a material property independent of geometry and loading condition, but propagation, otherwise, is strongly dependent to those parameters. Joyce and Link [72] performed a comprehensive experimental study on fracture resistance behavior for several different geometries. They argued about the sensitivity of the initiation toughness (given by J_{Ic}) and tearing modulus due to geometry configuration, loading mode and initial size defect. It turns out that the onset of crack growth is insensitive to geometry, but the tearing modulus (slope of R-curve) is subordinate to it. In Fig. 17c, albeit somewhat disperse, initiation of stable crack growth (given in δ_{Ic}) is $\delta_{Ic} \sim$ 0.2 mm for deep crack C(T)'s and $\delta_{Ic} \sim$ 0.4 mm for shallow crack SE(B). Meanwhile, the tearing modulus in terms of $\delta - T_m = mE/\sigma_y \cdot d\delta/da$ – measured at 1 mm of crack extension yields 517 for SE(B), 470 for C(T) 15% S.G. and 394 for C(T) 20% S.G. These results offer a compelling argument of the effect of side groove size on constraint level and consequently on fracture toughness for different type of specimens and loading modes. By reducing the net cross section of a deep crack C(T) – deemed as high constraint and then lower R-curve – in 5% the resulting R-curve increases as much as the R-curve of SE(B) for a large amount of crack growth ($\Delta a > 2$ mm).

5. Discussion

5.1. State of stress at fracture initiation

In the present approach plasticity and fracture are treated by separate (uncoupled), which make the calibration and application straightforward. The MMC model borrows the Lode angle dependency on plasticity from the Bai – Wierzbicki (B&W) plasticity model [52], and utilize the pressure dependency from the original MC model. After some mathematical manipulation, the first and third stress invariants of the Cauchy stress tensor are decoupled from the B&W model. The parameters, c_θ^s and c_θ^c become free variables and they are usually different from the original version. For simplicity $c_\theta^s = c_3$ and $c_\theta^c = 1$ when they are used as fracture criterion, but not recommendable when used for plasticity. This provides flexibility to the modeling technique by the incorporation of different types of plasticity models such as quadratic yield Hill'48, non-quadratic YLD2000-2D or CPB06 functions (see illustrative examples [57,74,75]). The apparent incompatibility as a result of the transformation of principal stresses in the stress space into the mixed space of the fracture criterion is overridden by decupling plasticity from fracture. This is done because fracture of metallic materials is a very complex phenomenological process and the original MC stress based model is not able to describe accurately without additional mathematical manipulation. When it is transferred to the mixed strain space for better resolution in predicting ductile fracture, certain modification is needed. It can be modified by either the MC stress based model or the plasticity model. To keep a simpler and elegant form of MC model, the former is selected.

Fig. 18a illustrates a direct comparison of the present model with the original MC failure criterion in the principal stress space. For reference purposes, the von Mises yield criterion is also included. The open circles are the stresses at which failure or fracture initiation occurs (measured displacement to fracture) extracted from simulations for flat specimen geometries. This representation is obtained from reversing back Eq. (5) and solving for the equivalent stress as a function of η and $\bar{\theta}$. By setting $c_3 = 1$ the original MC stress based is recovery (solid blue line) and the MMC is obtained by setting the free parameters to those given in Table 2 (black solid line). Indeed, the original MC model provides an adequate approximation for shearing and tensile plane strain experiments but fail slightly to predict fracture initation for biaxial and uniaxial tension loading. This is because the MC formulation is based basically on the maximum shear stress principle with pressure sensitive effect included. The cutting plane at which this failure criterion act is independent of intermediate principal stress (ordered σ_2), thus forming vertexes in the first and second quadrants. In other words, the dependence of failure relies on the combination of the maximum and minimum principal stresses and the influence of the pressure-sensitive first invariant, resulting in an asymmetric six sided polygon projection on the deviatoric plane [76]. This restriction is partially eliminated by incorporating into the MMC formulation the Lode angle parameter dependent c_3, which smooth the vertexes localized in the tension-tension and compression-compression quadrants. The parameter might be viewed as an operator to improve the fitting with the measured data. Likewise, its representation in the mixed strain-stress space denotes a rather discrepancy between both fracture criteria for tests with lower stress triaxiality levels ($\eta < 1$) (see Fig. 18b and c). The isopleths of Lode angle indicates that choosing the MC criterion for fracture prediction may induce some errors in the estimation for both tensile experiments (uniaxial and biaxial), but becomes negligible for triaxialities greater than unity. Meanwhile, isopleths of triaxiality in Fig. 18c bear about previous statement but reveal differences in the valley of the locus failure in the range of generalized shearing and plane strain condition ($\bar{\theta} \sim 1$). In general those discrepancies seemingly relevant for lower triaxialities (<5%) become trivial for notched round bars specimens for fracture initation prediction. This gives support of the current approach to predict fracture initation at different stress states and loading histories by keeping the Lode angle dependency, originally derived for plasticity, to enrich its predictive capabilities. Furthermore, the analysis also brings about one important issue regarding the coupling of plasticity with fracture. Based on previous results, one can assume that by separating plasticity from fracture gives rise more freedom for modeling different types of material with complex plasticity settings while the simplicity of the fracture criterion is maintained.

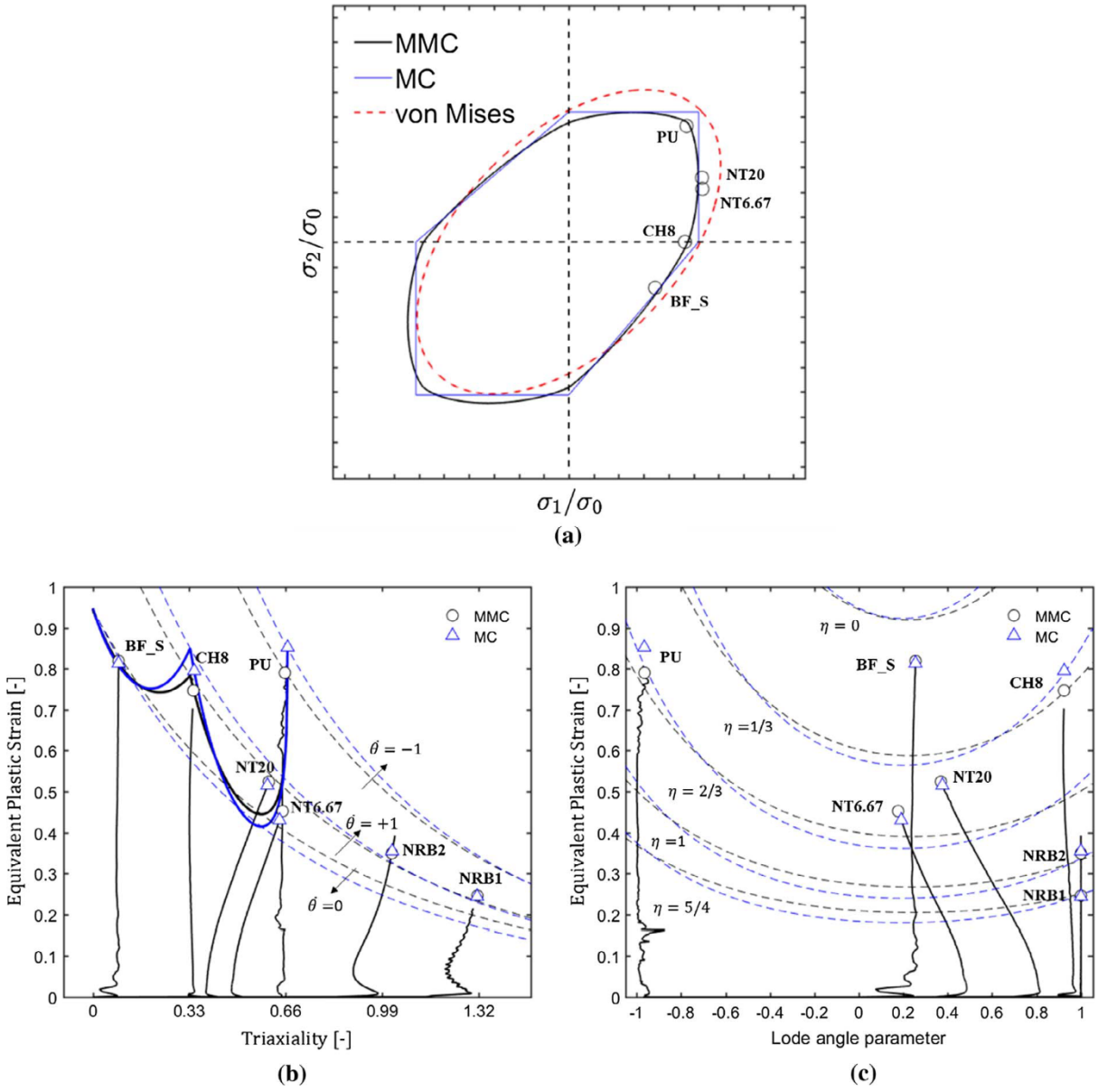

Fig. 18. 2D representations of state of stress for TC128 in: (a) principal stresses, (b) mixed equivalent plastic strain and stress triaxiality and (c) mixed equivalent plastic strain and Lode angle parameter. While the open symbols represent the fracture initiation points predicted by the model, the measured strain to fracture is indicated by the end of solid lines.

5.2. State of stress at fracture propagation

The near crack-tip fields are strongly influenced by blunting at the initial stage of deformation in ductile materials. This differs from the fact of crack initation in crack-free samples, where no initial strain-stress gradients are acting ahead of the tip. The concept of constraint plays an important role to understand the state of stress developed in the near-tip region. When a near-tip material point is under mode I loading, it is subjected to a large opening stress causing elongation on that direction and lateral contraction due to Poisson ratio. The surrounding material will prevent it from happen giving rise a triaxial stress state [78]. This constraint level will vary according to material properties, geometry, loading mode and initial crack length. Brocks and co-workers [79-81] found that there is a little influence of the constraint in thin-walled fracture specimens, since most of the strain energy goes to global plastic deformation and not to surface crack formation. For thick components, otherwise, the constraint level and its associate strain-stress gradient at the crack-tip will limit a specific set of modeling parameters to a certain type of structural components with similar constraint that those used for calibration. For instance, material parameters obtained from small crack-free scale lab specimens cannot be used for fracture initiation and propagation description (see illustrative examples [82,83]).

Void growth and coalescence mechanism depends strongly on the interaction between this locally phenomenological separation processes with the plastic dissipation occurring over large scale [33]. There is still an open question about what is the real contribution of each of these two processes to the total work of fracture. In that sense, under engineering point of view, Faleskog et al. [35,36] by means of porous plasticity models rationalized the process of material parameters calibration. Recognizing that a single RVE model is not enough to describe the complete range of stress triaxiality at which a given structural might be subjected, they included to the procedure the fracture resistance data in order to account for constraint. At the end of the day, this approach provides a rapid and efficient way to derive representative modeling parameters for real-world applications. One of the relevant features of porous models is the consideration of the post-peak stress softening, which comes naturally due to the mathematical formulation of the

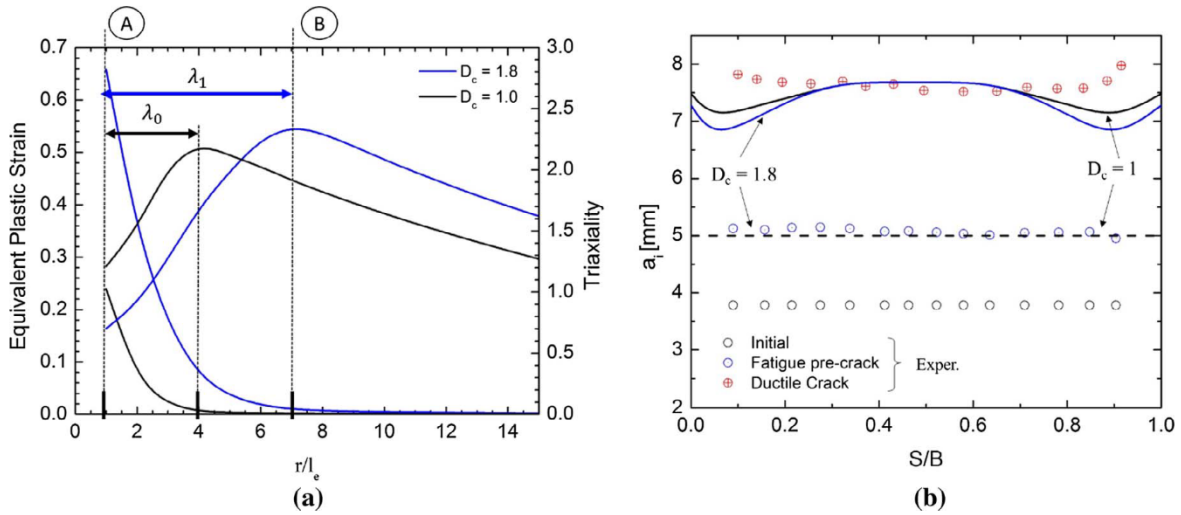

Fig. 19. (a) Spatial distribution of the state of stresses ahead of the growing crack measured in the midplane at the onset of stable crack propagation (δ_{Ic}); (b) experimental and numerical crack front measures of the side-grooved SE(B) specimens for $D_c = 1$ and 1.8. The distance ahead of crack-tip r is normalized with respect to element length in (a), whereas distance across thickness S is normalized regarding specimen thickness B.

constitutive equations. In other words, softening induced necking is implicitly treated as an internal variable as a result of void growth and coalescence mechanism. Not only localized necking can be predicted but also shear band formation due to shearing or plane strain in grooved square specimens.

Non-porous plasticity models with uncoupled fracture criteria overcome such limitation by a careful calibration procedure to capture post-necking behavior in finite strain problems. As shown in Fig. 3a, the use of a simple extrapolation hardening curve without internal damage variable might lead to significant error when extracting fracture parameters from the critical material point. For example, using a power law extrapolation ($\alpha = 1$) the model will under predict fracture initiation in around 20% with respect to the optimized flow curve ($\alpha = 0.6$). Likewise, for saturation type hardening law the extrapolation would lead to an over prediction estimation in around 40%. Therefore, even though non-porous plasticity models do not account for such damage mechanism and its effect on global load displacement response, the mathematical artifice employed here overtakes the underlying mechanism for post-necking behavior. It can be seen for the rest of experimental results in Fig. 3 the robustness of this technique to predict finite strain behavior not only for flat but also for notched round bars specimens. The latter are usually deemed as axisymmetric loading tension tests with high stress triaxiality concentration in which the main fracture mechanism is growth and coalescence of voids. Extension to crack propagation problems is achievable by considering the blunting into the fracture process. This has been done in many different ways for several researcher and investigating teams around the world. For example, the work done by Kim's group on problems involving complex cracked pipes. They use a modified Johnson-Cook as a fracture criterion with an uncoupled plasticity model to take account for plasticity. Even though unity indicates the initiation of fracture when damage indicator is considered, it does not account for propagation since a rapid plastic dissipation is observed with lower fracture resistance curve opposed of what is observed from the experiment. To sort the problem out, the damage indicator is calibrated by means of measured resistance data of standard C(T) specimen, which give rise values greater than unity for propagation. It has been noted that the predicted onset of stable crack propagation ($J_{0.2}$) value is mainly governed by damage indicator, whereas the ductile tearing modulus (T_m) by strain to fracture ($\bar{\varepsilon}_f$) parameters [84,85]. This assumption allows the model parameters being transferable to other similar constrained fracture specimens including some structural components.

In this work, the link between the local separation process involving hole growth and coalescence and plastic dissipation into background material has not been completely solved but was bridged by an elegant way through post-failure softening. The remarkable potentiality of the MMC model to predict initiation has been partially coupled with the plastic dissipation process experienced by material during stable crack growth. Experimental and numerical observations of the crack front serves as evidence of the suitability of the present approach to predict crack growth in different loading scenarios and constraint levels. In Fig. 19 the fracture process with and without post-failure softening is depicted along with the crack front measures. Assume, for instance, that the fracture process ahead of the tip in the midplane has a one-dimensional characteristic length λ that measures the distance between the point A where $D = D_c$ and the point B where the peak stress (triaxiality) is attained at $D > 0$ (see Fig. 19a).In the first case, where critical damage $D_c = 1$ (without post-failure softening, Eq. (9)) is assumed, λ_0 is around 4 denoting a small fracture process zone with lower peak triaxiality. This yields a lower resistance curve with rapid crack propagation as shown in Fig. 13. According to Tvergaard and Hutchinson [32] the required energy to initiate crack growth is equal to the work of separation per unit area. In this case, specifically, the separation work can be related to the strain energy expended to blunting the crack-tip prior initiation, which must equates the critical energy rate at initation given by critical δ_{Ic}. This is observed in Fig. 19a in blue solid lines, where the post-failure softening supplies the required energy for blunting by increasing the fracture process zone in almost ~ 2 times ($r/l_e \sim 7$) the previous zone λ_1, consequently increasing the peak triaxiality responsible for the dilatancy process ahead the tip.

The implications of applying post-failure softening into the constitutive formulation might not affect the crack front morphology as it is observed in Fig. 19b. The open colored symbols correspond to the measured crack extension in break-open specimens after test and solid/dash lines to the numerical simulations. The straight crack front after fatigue pre-cracking indicates the correct alignment between specimen and the testing assembly (rollers and axis actuator). In average the crack extended 2.5 mm from the pre-cracking front uniformly with some apparent reverse tunneling on the edges. This is confirmed by the numerical analysis for both configurations $D_c = 1$ and 1.8 whose results are plotted over the experiments. It is clear, that the use of post-failure softening has a negligible effect on the capabilities of MMC as a fracture criterion for thick-walled components, except the small lobes developed near the edges as a result of the side grooves presence. It has to mention that this features are not visible in the fracture surface not because are inexistence but probably they were removed accidentally when

breaking open the specimen with nitrogen as was discussed extensively above.

Finally, it should be mention about a major qualitatively differences between responses of thick components and thin sheet metals to external loads. In the former case there is a very strong interaction between the local separation process and global plastic dissipation. This interaction is conveniently accounted for by post-failure softening. At the same time such a strong interaction is absent in sheet metals for initiation and propagation of cracks.

6. Conclusion

In the present work a phenomenological approach along with strain softening algorithm was employed. The Modified Mohr-Coulomb (MMC) fracture criterion was used as a weighting function of the limit of ductility represented by a damage indicator function. The post-failure softening proves to be a useful tool to account for progressive damage evolution as deformation increases and thus predicting ductile fracture without losing the physical meaning of the present approach. Finally, these results serve as basis for further research including large-scale modeling of impact tank car simulations, which involves dynamics loads and ductile fracture propagation at different levels of triaxialities and loading conditions.

Acknowledgment

The work reported herein was supported by MIT Industrial Fracture Consortium with collaboration of Volpe the National Transportation Systems Center. The authors also want to acknowledge Professor Claudio Ruggieri and Professor Celso Pesce from University of Sao Paulo, Brazil for his support in facilitating the use of their loading frames for the testing program.

References

[1] T. Treichel, List of Accident-Caused Releases of Toxic Inhalation Hazard (TIH) Materialsfrom Tank Cars, 1965-2005, RSI-AAR Railroad Tank Car Safety Research and Test Project, RA 06-05, 2006.
[2] National Transportation Safety Board, Derailment of Canadian Pacific Railway Freight Train 292-16 and Subsequent Release of Anhydrous Ammonia Near Minot, North Dakota; January 18, 2002, Railroad Accident Report NTSB/RAR-04/01, 2004.
[3] National Transportation Safety Board, Collision of Union Pacific Railroad Train MHOTU-23 with BNSF Railway Company Train MEAP-TUL-126-D with Subsequent Derailment and Hazardous Materials Release, Macdona, Texas, June 28, 2004, Railroad Accident Report NTSB/RAR-06/03, 2006.
[4] National Transportation Safety Board, Collision of Norfolk Southern Freight Train 192 with Standing Norfolk Southern Local Train P22 with Subsequent Hazardous Materials Release at Graniteville, South Carolina, January 6, 2005, Railroad Accident Report NTSB/RAR-05/04, 2005.
[5] D.C. Tyrell, K. Jacobsen, B. Talamini, M. Carolan, Developing Strategies for Maintining Tank Car Integrity during Train Accidents, in: Proceedings of the 2007 ASME Rail Transportation Division Fall Technical Conference, RTDF2007, 1-10, 2007.
[6] Y.H. Tang, H. Yu, J.E. Gordon, D.Y. Jeong, A.B. Perlman, Analysis of Railroad Tank Car Shell Impacts using Finite Element Method, in: Proceedings of the 2008 IEEE/ASME Joint Rail Conference, JRC2008, 1-10, 2008.
[7] H.L. Yu, D.Y. Jeong, Application of a stress triaxiality dependent fracture criterion in the finite element analysis of unnotched charpy specimens, Theor. Appl. Fract. Mech. 54 (2010) 54–62.
[8] P.C. McKeighan, Mechanical Properties of Tank Car Steels Retired from the Fleet, Final Report, Southwest Research Institute, 1-331, 2008.
[9] Federal Railroad Administration, Development of New Federal Design Standards for Hazardous Materials Tank Cars to Benefit from Public-Private Partnership, U.S. Department of Transportation, FRA02-07, 1-17, 2007.
[10] D.C. Tyrell, D.Y. Jeong, K. Jacobsen, E. Martinez, Improved Tank Car Safety Research, in: Proceedings of 2007 ASME Rail Transportation Division Fall Technical Conference, RTDF2007-46013, 2007.
[11] R.H. Van Stone, et al., Microstructural aspects of fracture by dimpled rupture, Int. Metals Rev. 30 (4) (1985) 157–180.
[12] W.M. Garrison, N.R. Moody, Ductile fracture, J. Phys. Chem. Solids 48 (11) (1987) 1035–1074.
[13] D. Broek, The role of inclusions in ductile fracture and fracture toughness, Eng. Frac. Mech. 5 (1) (1973) 55–56.
[14] A.L. Gurson, Continuum theory of ductile rupture by void nucleation and growth: Part I - Yield criteria and flow rules for porous ductile media, J. Eng. Mater. Technol. 99 (1977) 2–15.
[15] M. Gologanu, J.B. Leblond, J. Devaux, Approximate models for ductile metals containing non-spherical voids—case of axisymmetric prolate ellipsoidal cavities, J. Mech. Phys. Solids, 41(11): 1723–1754.
[16] J.B. Leblond, G. Perrin, J. Devaux, An improved Gurson-type model for hardenable ductile metals, Eur. J. Mech. 14 (1995) 499–527.
[17] V. Tvergaard, J.W. Hutchinson, Two mechanisms of ductile fracture: void by void growth versus multiple void interaction, Int. J. Solids Struct. 39 (2002) 3581–3597.
[18] V. Tvergaard, A. Needleman, Analysis of the cup-cone fracture round tensile bar, Acta Metall. 32 (1) (1984) 157–169.
[19] F. Bron, J. Besson, A yield function for anisotropic materials Application to aluminum alloys, Int. J. Plast. 20 (4–5) (2004) 937–963.
[20] A. Benzerga, J. Besson, A. Pineau, Anisotropic ductile fracture, Acta Mater. 52 (15) (2004) 4623–4638.
[21] L. Xia, C.F. Shih, Ductile crack growth – I. A numerical study using computational cells with microstructurally-based length scales, J. Mech. Phys. Solids 43 (1995) 233–259.
[22] L. Xia, C.F. Shih, Ductile crack growth – II. Void nucleation and geometry effects on macroscopic fracture behavior, J Mech. Phys. Solids 43 (1995) 1953–1981.
[23] L. Xia, C.F. Shih, Ductile crack growth – III. Transition to cleavage fracture incorporating statistics, J. Mech. Phys. Solids 44 (1996) 603–639.
[24] L. Xia, C.F. Shih, J.W. Hutchinson, A computational approach to ductile crack growth under large scale yielding conditions, J. Mech. Phys. Solids 43 (1995) 389–413.
[25] C. Ruggieri, T.L. Panontin, R.H. Dodds, Numerical modeling of ductile crack growth in 3-D using computational cell elements, Int. J. Fract. 82 (1996) 67–96.
[26] D.Z. Sun, R. Kienzler, B. Voss, W. Schmitt, Application of micromechanical models to the analysis of ductile fracture resistance behavior, Numerical Methods in Fracture Mechanics, in: A.R. Luxmoore, D.R.J. Owen (Eds.), Proceedings of the 5th Int. Conf. held in Freiburg, FRG, 23–27 April, 1990, pp. 275–286, 1990.
[27] W. Brocks, D. Klingbeil, D. Kunecke, D.Z. Sun, Application of the Gurson model to ductile tearing resistance, in: M. Kirk, A. Bakker (Eds.), Constraint Effects in Fracture: Theory and Applications, ASTM STP 1244, American Society for Testing Materials, Philadelphia, PA, 1995, pp. 232–252.
[28] J.A. Begley, J.D. Landes, Serendipity and the J integral, Int. J. Frac. 12 (1976) 764–766.
[29] S.J. Garwood, Effect of specimen geometry on crack growth resistance, in: C.W. Smith (Ed.), Fracture Mechanics, ASTM–STP 667, American Society for Testing and Materials, 1979, pp. 511–532.
[30] J.W. Hancock, W.G. Reuter, D.M. Parks, Constraint and toughness parameterized by T, in: E.M. Hackett, K.H. Schwalbe, R.D. Dodds (Eds.), Constraints Effects in Fracture, ASTM STP 1171, American Society for Testing and Materials, 1993, pp. 21–40.
[31] J.A. Joyce, E.M. Hackett, C. Roe, Effects of crack depth and mode of loading on the J-R Curve behavior of a high strength steel, in: E.M. Hackett, K.H. Schwalbe, R.D. Dodds (Eds.), Constraints Effects in Fracture, ASTM STP 1171, American Society for Testing and Materials, 1993, pp. 21–40.
[32] V. Tvergaard, J.W. Hutchinson, The relation between crack growth resistance and fracture process parameters in elastic-plastic solids, J. Mech. Phys. Solids 40 (1992) 1377–1397.
[33] C.F. Shih, L. Xia, Modeling crack growth resistance using computational cells with microstructurally-based length scales, in: M. Kirk, A. Bakker (Eds.), Constraint Effects in Fracture, Theory and Applications, ASTM STP 1244, American Society for Testing and Materials, 1995, pp. 163–190.
[34] R.M. McMeeking, D.M. Parks, On criteria for J-dominance of crack-tip fields in large scale yielding, in: J.D. Landes, J.A. Begley, G.A. Clarke (Eds.), Elastic-Plastic Fracture, ASTM STP 668, American Society for Testing and Materials, 1979, pp. 175–194.
[35] J. Faleskog, X. Gao, C.F. Shih, Cell model for nonlinear fracture analysis – I. Micromechanics calibration, Int. J. Frac. 89 (1998) 355–373.
[36] X. Gao, J. Faleskog, C.F. Shih, Cell model for nonlinear fracture analysis – II. Fracture-process calibration and verification, Int. J. Frac. 89 (1998) 375–398.
[37] C. Ruggieri, F. Dotta, Numerical modeling of ductile crack extension in high pressure pipelines with longitudinal flaws, Eng. Struct. 33 (5) (2011) 1423–1438.
[38] F.B. Sarzosa, C. Ruggieri, A numerical investigation of constraint effects in circumferentially cracked pipes and fracture specimens including ductile tearing, Int. J. Press. Vessels Pip. 120–121 (2014) 1–18.
[39] B. Tanguy, T.T. Luu, G. Perrin, A. Pineau, J. Besson, Plastic and damage behaviour of high strength X100 pipeline steel: experiments and modelling, Int. J. Press. Vessels Pip. 85 (2008) 322–335.
[40] I. Scheider, A. Nonn, A. Völling, A. Mondry, C. Kalwa, A damage mechanics based evaluation of dynamic fracture resistance in gas pipelines, Proc. Mater. Sci. 3 (2014) 1956–1964.
[41] M.L. Wilkins, R.D. Streit, J.R. Reaugh, Cumulative-strain-damage model of ductile fracture: simulation and prediction of engineering fracture tests, Lawrence Livermore National Laboratory Report, UCRL-53058, 1980.
[42] G.R. Johnson, W.H. Cook, Fracture characteristics of three metals subjected to various strains, strain rates, temperatures and pressures, Eng. Frac. Mech. 21 (1) (1985) 31–48.
[43] Y. Bao, T. Wierzbicki, A comparative study on various ductile crack formation criteria, J. Eng. Mater. Technol. 126 (2004) 314–324.
[44] T. Wierzbicki, Y. Bao, Y.W. Lee, Y. Bai, Calibration and evaluation of seven fracture models, Int. J. Mech. Sci. 47 (4–5) (2005) 719–743.
[45] C.-K. Oh, Y.-J. Kim, J.-H. Back, W.-S. Kim, Development of stress-modified fracture strain for ductile failure of API X65 steel, Int. J. Fract. 143 (2007) 119–133.

[46] Y.H. Tang, H. Yu, J.E. Gordon, M. Priante, D.Y. Jeong, D.C. Tyrell, Perlman A.B., Analyses of Full-Scale Tank Car Shell Impact Tests, in: Proceedings of the 2007 ASME Rail Transportation Division Fall Technical Conference, RTDF2007, 1-10, 2007.
[47] H. Yu, D.Y. Jeong, Impact dynamics and puncture failure of pressurized tank cars with fluid-structure interaction: a multiphase modeling approach, Int. J. Impact Eng. 90 (2016) 12–25.
[48] Y. Bao, T. Wierzbicki, On fracture locus in the equivalent strain and stress triaxiality space, Int. J. Mech. Sci. 46 (2004) 81–98.
[49] J.W. Yoon, R.P.R. Cardoso, R.E. Dick, Puncture fracture in an aluminum beverage can, Int. J. Impact Eng. 37 (2010) 150–160.
[50] M. Lishaa, J. Chen, J.C.S. Yang, R. Kao, C. Orth, Impact of projectile of elliptical tank head, Pressure Vessel and Piping Conference, ASME, 1985.
[51] M. Brünig, S. Berger, H. Obrecht, Numerical simulation of the localization behavior of hydrostatic-stress sensitive metals, Int. J. Mech. Sci. 42 (2000) 2147–2166.
[52] Y. Bai, T. Wierzbicki, A new model of metal plasticity and fracture with pressure and Lode dependence, Int. J. Plast. 24 (2008) 1071–1096.
[53] X. Gao, T. Zhang, J. Zhou, S.M. Graham, M. Hayden, C. Roe, On the stress-state dependent plasticity modeling: significance of the hydrostatic stress, the third invariant of stress deviator and the non-associated flow rule, Int. J. Plast. 27 (2011) 217–231.
[54] Y. Bai, T. Wierzbicki, Application of extended Mohr-Coulomb criterion to ductile fracture, Int. J. Fract. 161 (2010) 1–20.
[55] M. Paredes, T. Wierzbicki, P. Zelenak, Prediction of crack initiation and propagation in X70 pipeline steels, Eng. Fract. Mech. 168 (2016) 92–111.
[56] D. Mohr, S.J. Marcadet, Micromechanically-motivated phenomenological Hosford-Coulomb model for predicting ductile fracture initiation at low stress triaxialities, Int. J. Solids Struct. 67–68 (2015) 40–55.
[57] K. Wang, L. Greve, T. Wierzbicki, FE simulation of edge fracture considering pre-damage from blanking process, Int. J. Solids Struct. 71 (2015) 206–218.
[58] X. Zhang, T. Wierzbicki, Characterization of plasticity and fracture of shell casing of lithium-ion cylindrical battery, J. Power Sources 280 (2015) 47–56.
[59] M. Dunand, D. Mohr, Hybrid experimental–numerical analysis of basic ductile fracture experiments for sheet metals, Int. J Solids, Struct. 47 (9) (2010) 1130–1143.
[60] M. Dunand, D. Mohr, Optimized butterfly specimen for the fracture testing of sheet materials under combined normal and shear loading, Eng. Fract. Mech. 78 (17) (2011) 2919–2934.
[61] C.C. Roth, D. Mohr, Ductile fracture experiments with locally proportional loading histories, Int. J. Plast. 79 (2016) 328–354.
[62] K. Kofiani, A. Nonn, T. Wierzbicki, New calibration method for high and low triaxiality and validation on SENT specimens of API X70, Int. J. Press. Vessels Pip. 111–112 (2013) 187–201.
[63] Y. Bai, Effect of the loading history on necking and fracture, PhD thesis, Massachusetts Institute of Technology, 2008, p. 1–262.
[64] A. Beese, M. Luo, Y. Li, Y. Bai, T. Wierzbicki, Partially coupled anisotropic fracture model for aluminum sheets, Eng. Fract. Mech. 77 (2010) 1128–1152.
[65] Y. Li, T. Wierzbicki, Prediction of plane strain fracture of AHSS sheets with post-initiation softening, Int. J. Solids Struct. 47 (17) (2010) 2316–2327.
[66] T. Wierzbicki, L. Xue, On the effect of the third invariant of the stress deviator on ductile fracture, Technical Report, Impact and Crashworthiness Laboratory, Massachusetts Institute of Technology, Cambridge, MA, 2005.
[67] American Society for Testing and Materials, Standard Test Method for Measurement of Fracture Toughness, ASTM E1820-13, 2013.
[68] D.F.B. Sarzosa, R.F. Souza, C. Ruggieri, J-CTOD relations in clamped SE(T) fracture specimens including 3-D stationary and growth analysis, Eng. Fract. Mech. 147 (2015) 331–354.
[69] D.F.B. Sarzosa, M. Verstraete, S. Hertelé, R. Denys, C. Ruggieri, Numerical simulation of ductile crack growth in medium wide plate specimens using 3-D computational cells, Eng. Fract. Mech. 168 (A) (2016) 26–45.
[70] L. Mathias, D.F.B. Sarzosa, C. Ruggieri, Effects of specimen geometry and loading mode on crack growth resistance curves of a high-strength pipeline girth weld, Int. J. Press. Vessels Pip. 111–112 (2013) 106–119.
[71] Y.J. Chao, X.K. Zhu, Constraint-modified J-R curves and its application to ductile crack growth, Int. J. Frac. 106 (2) (2000) 135–160.
[72] J.A. Joyce, R.E. Link, Effects of constraint on upper shelf fracture toughness, in: W.G. Reuter, J.H. Underwood, J. Newman (Eds.), Fracture Mechanics, ASTM STP 1256, American Society for Testing and Materials, Philadelphia, 1995, pp. 142–177.
[73] User Abaqus, Manual, RI, Rohde Island, 2014.
[74] M. Dunand, A.P. Maertens, M. Luo, D. Mohr, Experiments and modeling of anisotropic aluminum extrusions under multi-axial loading – Part I: plasticity, Int. J. Plas. 36 (2012) 34–49.
[75] Y. Jia, Y. Bai, Ductile fracture prediction for metal sheets using all-strain-based anisotropic eMMC model, Int. J. Mech. Sci. 155–116 (2016) 516–531.
[76] G.S. Schajer, Mohr-Coulomb failure criterion expressed in terms of stress invariants, J. Appl. Mech. 65 (1998) 1066–1068.
[77] M. Dunand, D. Mohr, On the predictive capabilities of the shear modified Gurson and the modified Mohr-Coulomb fracture models over a wide range of stress triaxialities and Lode angles, J. Mech. Phys. Solids 59 (2011) 1374–1394.
[78] T.L. Anderson, Fracture Mechanics: Fundamentals and Applications, third ed., CRC Press, Boca Raton, FL, 2005 33487-2742.
[79] I. Scheider, W. Brocks, Effect of the traction-separation law on the results of cohesive zone crack propagation analyses, Key Eng. Mater. 251–252 (2003) 313–318.
[80] T. Siegmund, W. Brocks, The role of cohesive strength and separation energy for modeling of ductile fracture, in: Fatigue and Fracture Mechanics, 30th Vol., ASTM STP 1360, 139-151, 2000.
[81] M. Anvari, I. Scheider, C. Thaulow, Simulation of dynamic crack growth using rate and triaxiality dependent cohesive elements, in: Proc. of the 16th Europe Conf. of Fract., 2006.
[82] I. Scheider, W. Brocks, Simulation of cup-cone fracture using cohesive model, Eng. Frac. Mech. 70 (2003) 1943–1961.
[83] C.R. Chen, O. Kolednik, I. Scheider, T. Siegmund, A. Tatschi, F.D. Fischer, On the determination of the cohesive zone parameters for the modeling of micro-ductile crack growth in thick specimens, Int. J. Fract. 120 (2003) 517–536.
[84] C.-S. OH, N.-H. Kim, Y.-J. Kim, J.-H. Baek, Y.-P. Kim, W.-S. Kim, A finite element ductile failure simulation method using stress-modified fracture strain model, Eng. Fract. Mech. 78 (2011) 124–137.
[85] K.-D. Bae, H.-W. Ryu, Y.-J. Kim, J.-S. Kim, Comparison of ductile tearing simulation with complex cracked pipe test data, J. Press. Vessel Technol. 139 (2017) 1–11.
[86] M. Paredes, C. Ruggieri, Further results in J and CTOD estimation procedure for SE(T) fracture specimens. Part I: weld centerline cracks, Eng. Fract. Mech. 89 (2012) 24–39.
[87] M. Paredes, Plastic limit load and its application to the fracture toughness testing for heterogeneous single edge notch tension specimens, Fatigue Fract. Eng. Mater. Struct. 37 (3) (2014) 265–279.